

Multi-frequency observations of PDS 70c

Radio emission mechanisms in the circum-planetary environment

Oriana Domínguez-Jamett¹, Simon Casassus^{1,2}, Haoyu Baobab Liu^{3,4}, Yuhiko Aoyama⁵, Miguel Cárcamo^{6,2}, Philipp Weber^{7,8,9}, Ondřej Chrenko¹⁰, Gabriel-Dominique Marleau^{11,12,13}, Barbara Ercolano^{14,15}, and Judit Szulágyi^{16,17}

(Affiliations can be found after the references)

Received 12/03/2025; accepted 25/07/2025

ABSTRACT

Aims. PDS 70c is a source of H α emission and variable sub-mm signal. Knowledge of the emission mechanisms may enable observations of accretion rates and physical conditions in the circum-planetary environment.

Methods. We report ALMA observations of PDS 70 at 145 GHz (Band 4), 343.5 GHz (Band 7) and 671 GHz (Band 9) and compare with archival data at 97.5 GHz (Band 3). The derived radio spectrum (SED) of PDS 70c is coeval within two months, and is interpreted in terms of analytic models of dusty and viscous disks (i.e. circumplanetary disks, CPDs). In a novel approach we include the free-free continuum from H I, metals (e.g. K I) and H⁺.

Results. New detections in Bands 3 (tentative at 2.6σ), 4 (5σ), and 7 (re-detected at 9σ) are consistent with optically thick thermal emission from PDS 70c (spectral index $\alpha = 2 \pm 0.2$). However, a non-detection in Band 9 breaks this trend, with a flux density falling below an optically thick extrapolation at 2.6σ . A viscous dusty disk is inconsistent with the data, even with the inclusion of ionised jets. Interestingly, the central temperatures in such CPD models are high enough to ionise H I, with huge emission measures and an optically thick spectrum that marginally accounts for the radio SED (within 3σ of Band 9). Since there is no room for steeper components (with $\alpha > 2$), the dust-to-gas ratio is strictly lower than 10^{-5} . By contrast, uniform-slab models suggest much lower emission measures to account for the Band 9 drop, with ionisation fractions $\sim 10^{-7}$, and an outer radius of ~ 0.1 au. Such conditions are recovered if the CPD interacts with a planetary magnetic field, leading to a radially variable viscosity $\alpha(R) \lesssim 1$ and central temperatures $\sim 10^3$ K that regulate metal ionisation. However, the H⁺ opacity still results in an optically thick SED, overshooting Band 9. We find that the optically thin turnover at $\gtrsim 600$ GHz is only recovered if a thin shocked layer is present at the CPD surface, as suggested by simulations. A photospheric shock or accretion funnels are ruled out as radio emission sources because their small solid angles require $T \sim 10^6$ K, which are unrealistic temperatures in planetary shock accretion.

Conclusions. The SED of PDS 70c collected here is optically thick up to Band 7 but probably (2.6σ) turns over towards Band 9. An optically thick spectrum can be explained by atomic plasma radiation from a magnetised disk, where the radio opacity stems from metal and H⁺ free-free. If so, PDS 70c is depleted of sub-mm-emitting dust by a factor of at least 1000. However, the turn-over can only be accounted for by H I free-free from an accretion shock at the surface of a CPD.

Key words. protoplanetary disks – circumplanetary disks – stars: individual: PDS 70 – techniques: interferometric – radio emission mechanism

1. Introduction

PDS 70 hosts two protoplanets detected in direct imaging, and probably even three (Keppler et al. 2018; Haffert et al. 2019; Wang et al. 2021; Christiaens et al. 2024; Hammond et al. 2025). Atacama Large Millimeter Array (ALMA) observations of PDS 70 resulted in the detection of a possible circumplanetary disk (CPD) around PDS 70c (Isella et al. 2019; Benisty et al. 2021), in the form of a point source in continuum emission at millimetre wavelengths in Band 7 (351 GHz), with a linear diameter of less than 1.2 au, or about one third the size of the Hill radius of the accreting protoplanet. This CPD is likely to play a crucial role in regulating the accretion process of PDS 70c. Its sub-mm flux density is variable by $\sim 40\%$ on time-scales shorter than 2 yr, and could be explained by the free-free continuum concomitant to the unresolved H α signal (Casassus & Cárcamo 2022) reported by (Haffert et al. 2019). For every proton-electron encounters leading to the recombination cascade, others will lead to free-free transitions.

The global hydrodynamic simulations of embedded thermal-mass bodies by Szulágyi et al. (2018), as well as the parametric viscous disk models by Zhu et al. (2018), suggest that higher

frequencies, such as those in ALMA Bands 9 and 10 (~ 671 GHz and ~ 850 GHz), are more suitable for CPD observations in the dust continuum. CPDs are predicted to be hotter than the surrounding circumstellar disk, and their (unresolved) emergent flux densities F_ν , in frequency, are thought to be mainly due to partially optically thick thermal dust with a spectral index of $\alpha \approx 3$ at ALMA frequencies, with α defined by $F_\nu \propto \nu^\alpha$.

However, if the radio signal from PDS 70c is mainly due to free-free emission, we should expect $\alpha \leq 2$. A rough approximation to partially-thick free-free emission can be obtained with an $1/r^2$ electron-density distribution, as in winds from early-type stars. The emergent free-free flux densities then follow a power-law spectrum $F_\nu \propto \nu^\alpha$ with $\alpha \sim 0.6$ (Wright & Barlow 1975).

The sub-mm detection of PDS 70c thus raises the questions: What is the nature of the emission, and why is PDS 70c detected in the sub-mm continuum, while PDS 70b is not? If the emission is due to thermal dust emission, a multi-wavelength analysis could shed light on the nature of the circum-planetary dust population. In turn, the free-free continuum component will inform directly on the planetary accretion process, without the large un-

certainties related to the levels of extinction that affect $H\alpha$ (e.g., Hashimoto et al. 2020).

In this study, we present new ALMA Band 4 (145 GHz), Band 7 (343 GHz) and Band 9 (671 GHz) observations of PDS 70, and compare them to archival data in Bands 3 data (97.5 GHz) from Doi et al. (2024), focusing on PDS 70c. Section 2 describes data acquisition, synthesis imaging and the extraction of the spectral energy distribution (SED) of PDS 70c. Sec. 3 analyses our results in terms of parametric disk models. Sec. 4 discusses which models can or cannot fit the data. Sec. 5 concludes.

2. Observations

2.1. Data acquisition

New ALMA observations of PDS 70 in Bands 4, 7 and 9 were obtained as part of ALMA project IDs 2022.1.00592.S and 2022.1.01477.S. Each band was acquired in an extended array configuration, labeled TM1, and a compact configuration, labeled TM2. An observation log is provided in Table 1. We also include in our analysis the archival datasets for Bands 3, from ALMA projects 2022.1.00893.S (Doi et al. 2024) and 2022.1.01477.S (Liu et al. 2024).

2.2. Imaging, self-calibration and alignment

The same imaging strategy as for the 2017 and 2019 Band 7 datasets (Casassus & Cárcamo 2022; Casassus et al. 2023) was extended to the other bands. For each band and array configuration, automatic (user-independent) self-calibration was performed using the *snow* package. This package replaces the CASA *tclean* imager (CASA Team et al. 2022) with *gputmem* (Cárcamo et al. 2018) in CASA self-calibration (i.e. in iterative calls to the *gaincal* and *applycal* CASA tasks). Image restoration was performed with a Briggs robustness parameter of $r = 2$. The *gaincal* solution interval was reduced by half in each iteration, starting with the scan length, and stopping when the peak signal-to-noise ratio (PSNR) decreases. The solution table with the highest PSNR was kept. After the phase calibration stage, a cycle of phase and amplitude self-calibration was performed to assess any PSNR improvements. During the antenna-gain calculations, using CASA task *gaincal*, all spectral windows are combined. Alignment was performed using the *VisAlign* package (Casassus & Cárcamo 2022; Casassus et al. 2023), selecting the datasets with the largest baselines as astrometric reference (i.e. TM1), and a final round of self-calibration with *snow* was applied to the concatenated dataset. The resulting images are summarised in Fig. 1.

For Band 3, we concatenated the two extended (TM1) configurations from projects 2022.1.00893.S, 2022.1.01477.S. The PSNR of these data are limited by thermal noise, and self-calibration did not produce any improvements. The datasets were acquired with different phase centers, and were aligned with *VisAlign* before concatenation. The reference was taken as 2022.1.00893.S. The resulting Band 3 continuum dataset yielded a PSNR of 13.6 with $r = 2$, limited by thermal noise. As shown in Fig. 1a, a bright point source is detected at the phase-center, which is coincident with the position of PDS 70 given by the GAIA ICRS coordinates (Gaia Collaboration et al. 2023). We therefore assume that this point source is due to accretion free-free emission on the central star, following Doi et al. (2024).

For Band 4, each array configuration (TM1 and TM2) was self-calibrated separately prior to concatenation. The PSNR for TM2 improved from 224 to 243 after one round of phase self-calibration and one round of combined phase and amplitude self-calibration. In contrast, TM1 is limited by thermal noise, with a PSNR of 49. An application of *VisAlign*, with TM1 as reference, showed that the pointing is very consistent in these datasets, with a shift smaller than 1 mas, and consistent intensities within 1%. Such remarkable consistency probably reflects the favourable observing conditions. Joint self-calibration after concatenation did not yield improvements in PSNR.

The new Band 7 data is coarser than in Benisty et al. (2021), with a restored beam in natural weights of $0''.102 \times 0''.082$ in TM1. We avoided concatenation with TM2 to preserve angular resolution. The PSNR of TM1 improved from 104 to 257 after two rounds of phase self-calibration, and reached 308 after amplitude and phase self-calibration. However, we selected the phase-only self-calibration for our final dataset, as the amplitude gains resulted in a drop in flux density for PDS 70 by 20%, compared to both TM2 and the phase self-calibrated TM1.

In Band 9, the PSNR for TM2 increased from 29.2, to 33.3 after two rounds of phase calibration, and to 111 after one round of combined amplitude and phase self-calibration. TM1 was affected by a low-spatial frequency modulation, probably caused by poor weather and resulting in noisy phases. We opted to discard baselines shorter than $0.4 M\lambda$. The uvrange-clipped dataset yielded a PSNR of 24, which did not improve with self-calibration. An application of *VisAlign* to align TM2 to TM1 resulted in a shift of $\Delta\alpha = 25.6$ mas along R.A., and $\Delta\delta = 0.13$ mas along Dec., with a correction in intensity scale of 78%. While seemingly large, the positional shift is within the pointing uncertainty of the TM2 dataset, which is about 1/10 of the beam or 15 mas (at 1σ). Likewise, the absolute flux calibration accuracy in Band 9 is around 10%. Failing to apply the positional shift to TM2 results in images of the concatenated dataset with a spurious excursion of the ring into the cavity. We applied the correction factor of 1/78% to TM1. Self-calibration of the concatenated dataset did not yield improvements.

While the star PDS 70 is readily picked-up in Band 3, it bears no clear counterparts in the other bands. There may be a point-source associated with the star in Band 4, where the central emission appears to be split into 4 blobs in the deconvolved image of Fig. 1f, one of which coincides with the expected stellar position with 3σ flux. The other blobs are offset by ~ 50 mas, which is too large to account for by a pointing error in Band 4, given by $\sim 1/10$ of the Band 4 TM1 beam, or ~ 8 mas. We fit elliptical Gaussians to extract the stellar flux densities. Comparing $24 \pm 5 \mu\text{Jy}$ in Band 3, with $18 \pm 4 \mu\text{Jy}$ in Band 4, corresponds to a spectral index $\alpha = -0.7 \pm 0.8$, which is too noisy to distinguish partially-thick free-free emission ($\alpha \sim 0.6$, Wright & Barlow 1975), variability, or a synchrotron component. We apply *VisAlign* to check on the inter-band alignment, using Band 3 as reference given the detection of the star. Band 4 is shifted by $\Delta\alpha = -4.9 \pm 1.1$ mas, $\Delta\delta = -13 \pm 1.1$ mas, which is within the pointing errors in Band 4.

There is no counterpart of the star in Bands 7 or 9 with which to cross check on the inter-band alignment, and the ring appears dramatically different in radius and width compared to Band 3, hampering the application of *VisAlign*. We simply rely on the absolute pointing accuracy, of ~ 10 mas in Band 7 and ~ 5 mas in Band 9.

Table 1. Observation log of the new Band 4 and Band 9 observations of PDS 70.

Band /dataset	UT Date	ToS ^a (s)	Elev. ^b (deg)	PWV ^c (mm)	Phase ^d rms (deg)	Min BL ^e (m)	Max BL ^f (m)
4/TM1	2023-07-09	5521	70.2	0.6	6.2	113	12752
4/TM1	2023-07-09	5485	66.3	0.6	5.6	113	12752
4/TM1	2023-07-10	5478	67.2	1.2	8.8	226	13814
4/TM1	2023-07-12	5511	66.3	0.6	8.8	226	15238
4/TM2	2023-04-30	3865	71.2	1.3	5.6	15	2517
7/TM1	2023-05-23	10213	69	0.9	6.9	78	3638
7/TM1	2023-06-01	10128	57	0.5	6.3	27	3638
7/TM1	2023-06-02	9560	68	0.5	5.8	27	3638
7/TM1	2023-06-03	10109	62	0.7	10.3	27	3638
7/TM1	2023-06-04	9484	66	0.6	8	27	3638
7/TM1	2023-06-07	10113	66	0.6	8	77	3638
7/TM1	2023-06-08	10135	69	0.7	6.4	27	3638
7/TM1	2023-11-27	10184	57	0.7	11.5	31	3697
7/TM1	2023-11-28	10355	59	0.8	10.0	31	3638
9/TM1	2023-06-11	7197	70.5	0.5	61	79	4614
9/TM2	2023-12-21	7171	68.4	0.5	52	15	1397

Notes. ^(a) Time on source. ^(b) Average elevation. ^(c) Column of precipitable water vapor. ^(d) Root-mean-square (rms) phase noise. ^(e) Minimum baseline. ^(f) Maximum baseline.

Table 2. Multi-frequency imaging properties of the restored images in Fig. 1.

Bands	3	4	7	9
r^a	1.0	1.0	0.0	2.0
Ω_b^b	$0''.077 \times 0''.070 / -64 \text{ deg}$	$0''.075 \times 0''.064 / -48 \text{ deg}$	$0''.059 \times 0''.050 / -75 \text{ deg}$	$0''.054 \times 0''.045 / 78 \text{ deg}$
σ^c	4.68	4.06	14	115

Notes. ^(a) Briggs parameter used for the restoration. ^(b) The beam major axis (bmaj), minor axis (bmin) and direction (bpa) are in the format bmaj×bmin/bpa. ^(c) Noise, in $\mu\text{Jy beam}^{-1}$, in the restored images, as given by the root-mean-square dispersion in the imaging residuals.

Table 3. Point source measurements for PDS 70c.

Band	3	4	7	7	7	9
Date	2023-07-02	2023-04-30	2017-12-02	2019-07-27	2023-05-23	2023-06-11
ν/GHz	97.5	145	350.1	350.1	343.5	671
Flux / μJy	12 ± 4.7	21.4 ± 4.1	37 ± 23.9	118.5 ± 16.6	121 ± 13	143 ± 115^a
$\delta\text{RA}^b / \text{mas}$	-207.2 ± 9	-222 ± 8	—	-218 ± 5	-212.7 ± 10.2	—
$\delta\text{DEC}^c / \text{mas}$	-4.4 ± 9	-5 ± 8	—	27 ± 5	-12.1 ± 10.2	—

Notes. Uncertainties on the position (relative to PDS 70) are taken as 1/10 the clean beam major axis, in natural weights. ^(a) For Band 9 we show a measurement of the intensity of the peak in a region centred on its expected position. ^(b) Offset along right-ascension. ^(c) Offset along declination.

2.3. Point source measurements of PDS 70c

We searched for radio counterparts to PDS 70b, c and d by estimating their positions at the epochs of observations, under the assumption that their orbit is circular around a $0.97 M_\odot$ star, and in the plane of the disk, with position angle $\text{PA} = 160 \text{ deg}$, and inclination $i = 130 \text{ deg}$ (e.g. Casassus & Cárcamo 2022). The two circles in each of the images in Fig. 1 are centred on the positions of b and d, using the coordinates provided by Wang et al. (2021, from UT2020-02-10) and Christiaens et al. (2024).

No counterparts were detected for PDS 70b or d, at any frequency. However, we did find counterparts to PDS 70c in Bands 3 and 4. In Band 3 a point-source signal at 2.6σ in the restored map is found at $\Delta\alpha = 9 \pm 8 \text{ mas}$, $\Delta\delta = -1 \pm 8 \text{ mas}$, from the expected position of PDS 70c, as estimated with an elliptical Gaussian fit to the Band 7 source (see Table 3). Given the pointing uncertainties in Band 7 (of $\sim 5 \text{ mas}$), the uncertainties in the orbit, and the faint Band 3 counterpart which can be modu-

lated by thermal noise, a shift of 9 mas is well within the errors. We record the peak intensity in Jy beam^{-1} as a measurement of the point-source flux, and set its uncertainty to the noise in the residual image.

In Band 4, a point-source at 5.2σ is found at $\Delta\alpha = 7 \pm 7 \text{ mas}$, $\Delta\delta = 2 \pm 7 \text{ mas}$ from the expected position of PDS 70c. The centroid of the point-source was estimated with an elliptical Gaussian fit in the deconvolved image. Our choice of a Briggs parameter of $r = 1$ in Sec. 2.2 for image restoration is a compromise in terms of resolution to separate PDS 70c from the outer ring and PSNR.

PDS 70c is very conspicuous in the new Band 7 data, especially in the deconvolved image of Fig. 1g. The shift from its expected position is $\Delta\alpha = 13 \pm 12 \text{ mas}$, $\Delta\delta = -6 \pm 12 \text{ mas}$. But its flux density is difficult to measure because of confusion with the cavity wall. The peak on PDS 70c, in the restored map of Fig. 1c, is $111 \pm 14 \mu\text{Jy}$, and a Gaussian fit to the deconvolved

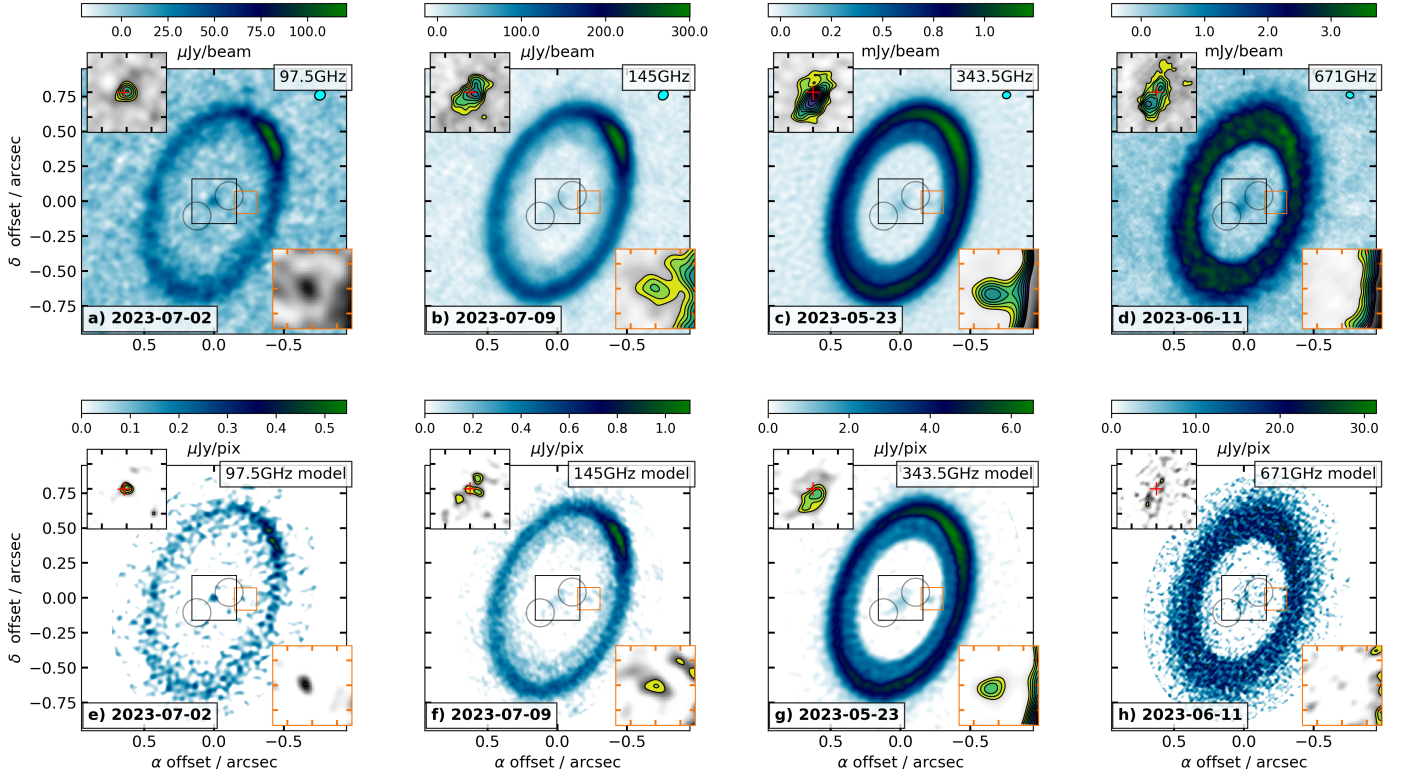


Fig. 1. Multi-frequency imaging of PDS 70. The black insets, at the top left of each image, zoom on the central region (with tick-marks separated by $0''.1$) while the orange insets, at the bottom right, zoom on the expected position of PDS 70c for circular Keplerian rotation around a $0.97 M_{\odot}$ star (with tick-marks at $0''.05$). The red plus symbol in the central inset marks the nominal position of the star. In all insets the linear grey scale stretches over the range of intensities in each region, and the contour levels start at 3σ and are incremented in units of σ . Intensities within each contour level are color-coded differently. The two circles are centered on the positions of PDS 70b and PDS 70d (no radio counterparts are detected). Images in *a*) to *d*), along the top row, correspond to restorations of the corresponding non-parametric model images (that fit the visibility data), in *e*) to *h*), along the bottom row. A beam ellipse in *a*) to *d*) is shown in blue, on the top right. The pixel size in the model images is fixed at $4 \times 4 \text{ mas}^2$. For each band the Briggs parameter used for the restoration, the clean beam and the noise can be found in Table 2.

map of Fig. 1g yields $157 \pm 27 \mu\text{Jy}$. We report the weighted average, $121 \pm 13 \mu\text{Jy}$.

Intriguingly, no counterparts of PDS 70c were found in Band 9, and the flux was obtained with the intensity of the peak in a region centred on its expected position, and with a radius given by 3 times the rms pointing accuracy (of $\sim 5 \text{ mas}$). We did not attempt to correct for the diffuse emission near the edge of the cavity, which would lower the flux density reported in Table 3. As the absence of PDS 70c in Band 9 is particularly surprising, we performed point-source injections tests in the uv -plane, using optically thick spectra tied to Band 7. As shown in Fig. 2, such point sources should indeed be detectable, at least in the form of a protrusion of the cavity wall.

The Band 3 and Band 9 flux density measurements of PDS 70c presented here do not correspond to detections. However, their exclusion from the resulting SED would represent a severe loss of information. In turn, incorporating these non-detections as 2 or 3σ upper limits injects a bias in attempts to fit this SED, by setting the expectation value for the flux densities to zero (or any other arbitrary value). The prior knowledge of the existence of PDS 70c, and of its orbit, is incorporated by reporting the peak flux density, within a beam, at the expected location of PDS 70c. This approach was referred to as “forced photometry” by Samland et al. (2017), for the incorporation of non-detections in the SED of 51 Eri b.

With the flux measured in different bands, we use the spectral index α as a useful indicator of the emission mechanisms at radio

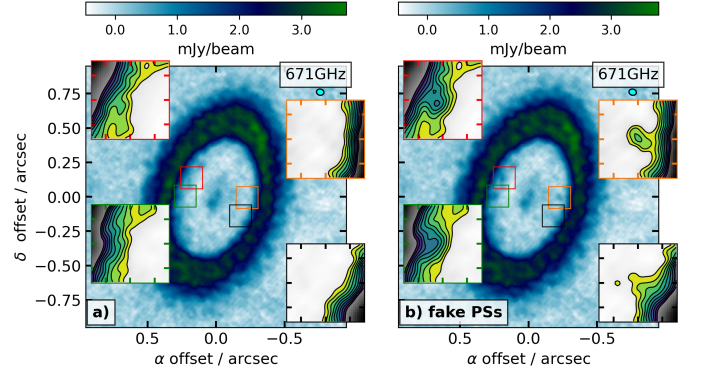


Fig. 2. Point-source injections tests in Band 9. *a*) Same as Fig. 1, with additional insets. *b*) Same as *a*) but with four point sources, injected at the centre of each inset, and with a flux density corresponding to an optically thick extrapolation of the Band 7 flux density for PDS 70c.

frequencies,

$$\alpha(\nu) = \frac{d \ln(F_{\nu})}{d \ln(\nu)}. \quad (1)$$

We estimate α in PDS 70c using the measurements from Table 3, by comparing frequency pairs,

$$\alpha_{\nu_1}^{\nu_2} = \frac{\ln(F_{\nu_2}/F_{\nu_1})}{\ln(\nu_2/\nu_1)}, \quad (2)$$

and by fitting a power-law to more than two frequency points,

$$F_\nu = F_{\nu_0} \left(\frac{\nu}{\nu_0} \right)^\alpha, \quad (3)$$

with ν_0 fixed to 145 GHz.

A summary of different spectral index estimates is given in Table 4. Measurements involving Bands 3, 4, 7 and 9 in 2023 are spread within two months (except for the Nov. 2023 execution blocks in Band 7), and are the least biased by variability compared to the 2017 and 2019 data.

2.4. Variability study

The new Band 7 data were acquired in nine executions blocks spanning seven epochs, and each of these execution blocks reached thermal noise levels of $\sim 20\text{--}30 \mu\text{Jy beam}^{-1}$, in natural weights, which should be deep enough to detect PDS 70c. However, the natural weight beams, of $\sim 0''.12$, are too coarse to separate PDS 70c from the bright ring. We therefore proceeded to subtract the disk emission from the visibility data. In this case we opted to work on the visibility data after amplitude and phase self-calibration, which ensures a consistent flux scale across all epochs. This was ascertained by aligning all epochs to 23-May-2023 with VisAlign, resulting in positional shifts of less than 1 mas, and amplitude shifts of less than 1%. We prepared a disk image with the `gputmem` model of the resulting visibilities (same as in Fig. 1g), and subtracted PDS 70c with an elliptical Gaussian fit. Simulated visibilities on this model image were then computed with the `pyralysis` package (Casassus & Cárcamo 2022) and subtracted from the observations. The dirty maps of the residuals are shown in Fig. 3, in natural weights (and also computed with `pyralysis`). The residual intensities are not perfectly thermal, as the model image fits the averaged dataset, not individual executions blocks. Nevertheless, PDS 70c stands out as the brightest residual in all epochs.

The technique of uv -plane subtraction of the disk signal allows to build visibility data containing mostly the signal from PDS 70c only, and with a consistent flux scale. We can thus proceed with point-source fits in the uv -plane, fixed at \mathbf{x}_0 , the position of the elliptical Gaussian centroid used to subtract PDS 70c, but with the best-fit amplitude (obtained by weighted least squares minimisation):

$$F_\nu = \frac{\sum_k \omega_k \Re \left[V_k^\circ \exp(-2\pi i \mathbf{u} \cdot \mathbf{x}_0) \right]}{\mathcal{A}_0 \sum_k \omega_k}, \quad (4)$$

where $\Re[\cdot]$ denotes the real part, and with rms uncertainties

$$\sigma(F_\nu) = \frac{1}{\mathcal{A}_0 \sqrt{\sum_k \omega_k}}, \quad (5)$$

where the sums extend over all observed visibilities V_k° at frequency ν , with weights ω_k , and with primary beam attenuation $\mathcal{A}_0 = \mathcal{A}(\mathbf{x}_0)$ at the position \mathbf{x}_0 . We stress that while this technique is suitable for a variability study, it cannot be used to extract the flux density of the point-source in the concatenated dataset, since the model image fits this point source.

In practice we collapsed all channels in each spectral window, yielding 4 flux-density measurements. The weighted average flux density at each epoch is recorded in Fig. 4. The weighted average is $130 \pm 4 \mu\text{Jy}$, with a weighted scatter of 9.3%. Therefore the flux density of PDS 70c is constant across all 7 epochs

within $\sim 10\%$. A non-detectable variability of the Band 7 flux densities the PDS 70c in 2023, is also consistent, given the uncertainties, with the conclusion from Fasano et al. (2025), who compared measurements in 2019, 2021, and 2023. The Band 4–Band 7 spectral index derived here is consistent with the Band 6–Band 7 index reported by Fasano et al. (2025).

3. Analysis

From the spectral indices in Table 4, we note that optically thick emission, that is $\alpha \gtrsim 2$, is consistent with the data between Bands 3 and 7 but only marginally consistent when we add Band 9. This is very difficult to reconcile with dust emission, where the emergent total (unresolved) flux densities mix optically thick and thin regions, resulting in spectral indices larger than 2.5 and closer to 3, depending on the choice of grain population (Zhu et al. 2018; Shibaike et al. 2025). In fact, a blackbody fit to Bands 3, 4 and 7 predicts $465 \pm 42 \mu\text{Jy}$ in Band 9, and overshoots the observation by 2.6σ .

The non-detection of PDS 70c in Band 9 is intriguing, as CPD models predict a bright signal at such short wavelengths, and favour Band 9 for CPD searches (Szulágyi et al. 2018; Zhu et al. 2018). It seems unlikely that this non-detection is caused by variability, given Sec. 2.4, and since PDS 70c is readily detected in Bands 4 and 7 at $\sim 5 \sigma$ and $\sim 9 \sigma$ respectively. Instead, the multi-frequency data suggest that free-free emission, rather than the thermal dust component, may originate the PDS 70c radio signal. In this Section we analyse our results in terms of simple parametric models of the radio signal from CPDs, which we use to reproduce the measurements from Bands 3, 4, 7 and 9.

3.1. PDS 70c SED models

The lack of CPD detection in Band 9 may be indicative of free-free radiation. To test this hypothesis, we extended the parametric CPD model proposed by Zhu et al. (2018) to include the free-free emission expected from the CPD itself (here we consider the radio free-free contributions from all species). For completeness we reproduce here some of the formulae from Zhu et al. (2018), before incurring in some approximations and including our extensions.

The model from Zhu et al. (2018) incorporates H I free-free emission in the form of a jet. For this component, we use the formula from Anglada et al. (2018) to estimate the emission of a circum-stellar disk at 1 cm:

$$\left(\frac{F_{1\text{cm, jet}} d^2}{\text{mJy kpc}^2} \right) = 10^{-1.9} \left(\frac{L_{\text{acc}}}{L_\odot} \right)^{0.6}, \quad (6)$$

with

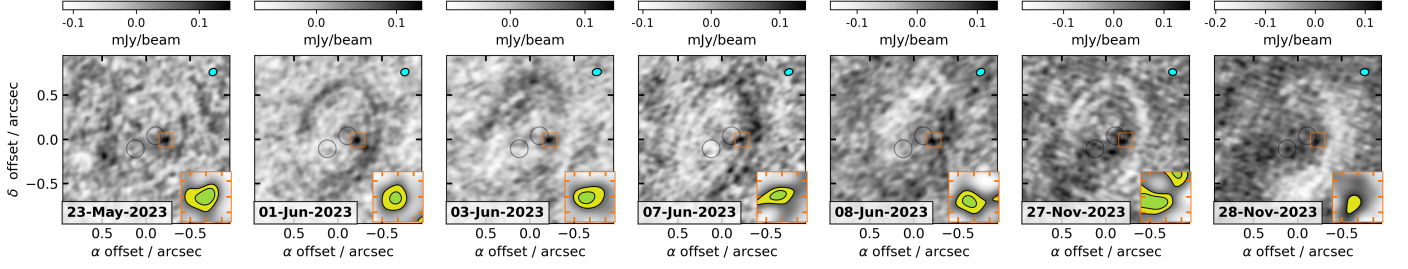
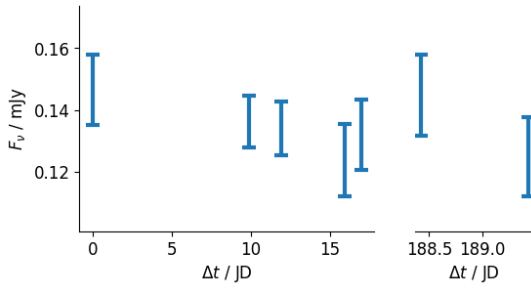
$$L_{\text{acc}} = \frac{GM_p \dot{M}_p}{2R_{\text{in}}}, \quad (7)$$

where M_p is the mass of the planet, \dot{M}_p the accretion rate onto it, and R_{in} the inner edge of the CPD.

The 1 cm flux density of the jet may be extrapolated to mm-wavelengths under the hypothesis of a power-law spectrum. If the jet is partially optically thick, an upper limit is set on the spectral index with $\alpha_{\text{jet}} = 0.4$ (Carrasco-González et al. 2016). In the case of an optically thin jet, $\alpha_{\text{jet}} = -0.1$. It should be borne in mind that these formulae were developed for stellar jets, rather than protoplanets, and that they are being extrapolated into the planetary mass regime.

Table 4. Spectral indices for PDS 70c.

Bands	B7/B3	B7/B4	B7/B4/B3	B9/B7/B4/B3
α	1.84 ± 0.32	2.01 ± 0.22	1.96 ± 0.22	1.73 ± 0.17


Fig. 3. Dirty maps in natural weights of the residual Band 7 visibilities, after subtraction of the disk. The grey scale stretches over the full intensity scale, and for each of seven epochs. The inset zooms into PDS 70c, with contours at 90 and 120 $\mu\text{Jy beam}^{-1}$, fixed for ease of comparison across epochs. As in Fig. 1, the circles are centred on PDS 70b and d, and are drawn here to ease the search of any variable counterparts.

Fig. 4. Flux density of PDS 70c at 343.5 GHz (Band 7), as a function of Julian day. The scatter is consistent with the uncertainties.

The parametric CPD model from [Zhu et al. \(2018\)](#) calculates the radio emission based on the disk accretion rate \dot{M}_p and viscosity parameter α . Prior to applying this model to PDS 70c, we made sure to reproduce the tables from [Zhu et al. \(2018\)](#) for the boundary layer case (this assumes that the planet accretion luminosity dominates over the central brightness of the planet itself), and in the Rayleigh-Jeans approximation for consistency.

We opted for a planetary mass $M_p = 4 M_{\text{Jup}}$, given the upper limit of $4.9 M_{\text{Jup}}$ ([Doi et al. 2024](#), based on a circum-stellar disk viscosity parameter of $\alpha = 10^{-3}$) and the restriction $4 M_{\text{Jup}} < M_p < 12 M_{\text{Jup}}$ ([Haffert et al. 2019](#)). PDS 70 is at a distance of 112.3 pc ([Gaia Collaboration et al. 2023](#)), and we adopted a planetary orbital radius for PDS 70c of 34 au ([Haffert et al. 2019](#)), implying an outer CPD radius $R_{\text{out}} = 1/3 R_{\text{Hill}} \sim 1.23$ au ([Quillen & Trilling 1998](#)), corresponding to angular size of $\Theta = 0''.011$. The radius of the planet R_p and the inner radius R_{in} were both set to $1 R_{\text{Jup}}$ following [Zhu et al. \(2018\)](#). This choice does not affect our results significantly since, as we will see for the CPD models, most of the flux does not come from the inner region.

The posterior distributions on the free parameters of our SED models were sampled with the *Nautilus* package ([Lange 2023](#)), which implements nested sampling aided by neuronal networks. We assumed flat priors in logarithm, with very wide boundaries.

We considered four models for the observed SED. Firstly, we considered only the dust component from the CPD. Secondly, we included an optically thin jet. Thirdly, we included an optically thick jet. Finally, we included free-free emission from the disk itself, using an α -constant disk and a magnetic disk. We also guided our analysis using a uniform slab model, adding the contribution of free electrons from metals in the magnetic disk.

3.2. Dust component of the CPD

In the absence of a jet, a strong degeneracy was observed between the parameters for smaller values of the accretion rate \dot{M}_p and larger values of the viscosity parameters α . For example, using synthetic data obtained with the parametric model of [Zhu et al. \(2018\)](#), for Bands 3, 4, 7 and 9 with $\dot{M}_p = 10^{-9} M_{\text{Jup}} \text{ yr}^{-1}$ and $\alpha = 10^{-3}$, we obtained the orange corner plot shown in Fig. 5, revealing that the important parameter is the ratio between these two parameters. By contrast, in the case of a larger accretion rate $\dot{M}_p = 10^{-5} M_{\text{Jup}} \text{ yr}^{-1}$ and the same viscosity parameter, the flux depends solely on the accretion rate, as can be seen in the grey corner plot shown in Fig. 5 (as noted by [Zhu et al. 2018](#)).

The degeneracy between \dot{M}_p and α can be understood by writing the emergent flux density,

$$F_\lambda = \frac{1}{d^2} \int_{R_{\text{in}}}^{R_{\text{out}}} B_\nu(T_b) 2\pi R dR, \quad (8)$$

where B_ν is the Planck function (we use the full blackbody function rather than the Rayleigh-Jeans approximation because the disk could reach low temperatures), d is the distance to PDS 70, and the brightness temperature is given by [Zhu et al. \(2018\)](#),

$$T_b = \begin{cases} \left(\frac{3}{8} \frac{\kappa_R}{\kappa_{\text{mm}}} T_{\text{eff}}^4 + T_{\text{ext}}^4 \right)^{1/4} & \text{if } \tau_{\text{mm}} > 0.5, \\ 2T_c \tau_{\text{mm}} & \text{if } \tau_{\text{mm}} < 0.5. \end{cases} \quad (9)$$

The Rosseland mean opacity was chosen to be constant, at the nominal value $\kappa_R = 10 \text{ cm}^2/\text{g}$ (as in [Zhu et al. 2018](#)). The dust opacity is $\kappa_{\text{mm}} = 3.4\zeta \times \frac{0.87 \text{ mm}}{\lambda} \text{ cm}^2/\text{g}$ ([Andrews et al. 2012](#), with ζ the dust-to-gas ratio usually set as 0.01), and the optical depth $\tau_{\text{mm}} = \kappa_{\text{mm}} \Sigma/2$. The effective temperature T_{eff} is the temperature that the surface of the viscous disk would radiate if it were a blackbody ([Hartmann 1998; Zhu et al. 2018](#)),

$$T_{\text{eff}}^4 = \frac{3GM_p \dot{M}_p}{8\pi\sigma R^3} \left[1 - \left(\frac{R_{\text{in}}}{R} \right)^{1/2} \right], \quad (10)$$

and the external temperature is $T_{\text{ext}}^4 = T_{\text{floor}}^4 + T_{\text{irr}}^4$, where T_{floor} is the background temperature in the environment of the CPD and T_{irr} is the temperature-equivalent irradiation flux from the planetary photospheric luminosity.

The background temperature in the circum-stellar disk environment surrounding the CPD, T_{floor} , is a crucial parameter as

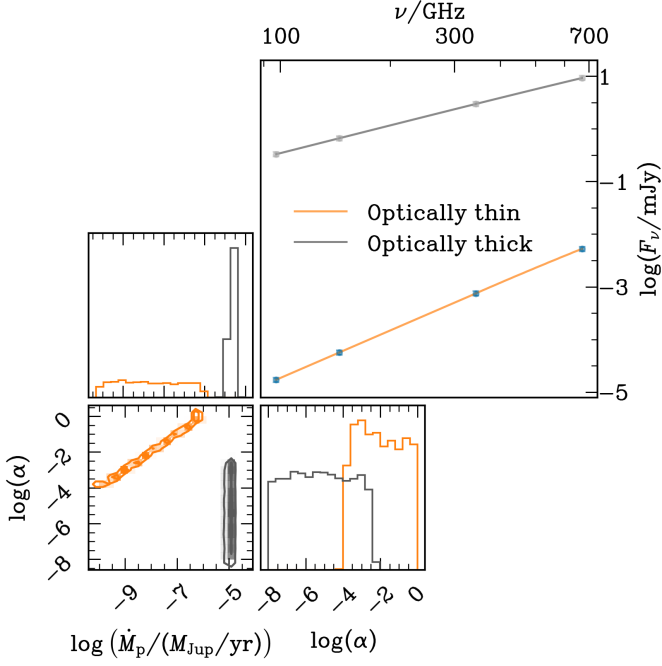


Fig. 5. Corner plot for synthetic data. The orange posteriors show the synthetic optically thin case, calculated with $\dot{M}_p = 10^{-9} M_{\text{Jup}} \text{ yr}^{-1}$ and $\alpha = 10^{-3}$. The outcome illustrates the degeneracy between \dot{M}_p and α inherent to the parametric CPD model of [Zhu et al. \(2018\)](#). The grey posteriors show the synthetic optically thick case, calculated with $\dot{M}_p = 10^{-5} M_{\text{Jup}} \text{ yr}^{-1}$ (and the same $\alpha = 10^{-3}$). Both synthetic SEDs were obtained using only the dust component of the CPD model following [Zhu et al. \(2018\)](#), with errors set to 10% of the flux.

it sets the floor temperature in the CPD. We used $T_{\text{floor}} = 27 \text{ K}$, which is obtained by extrapolating the dust physical conditions in the outer ring obtained by multi-frequency SED fits (these dust diagnostics will be documented in a forthcoming article). The azimuthally-averaged temperature profile of 21 K at a deprojected radius of $0.5''$ (56 au), was extrapolated to the position of PDS 70c, at $0.3''$ (i.e. 34 au) under the assumption of a temperature profile of $R^{-1/2}$. In practice, the uniform-slab dust diagnostic suggest a much higher temperature, as a power-law fit to the dust temperatures in the outer ring yields 49.9 K at 34 au . However, we adopt the value of 27 K in a conservative approach, as a lower value widens the range of possible dust temperatures in the CPD. For comparison, the peak brightness temperature in Band 9, of 14.7 K at 67 au , would translate to 21 K at 34 au with a $R^{-1/2}$ temperature profile. Additionally, the mid-plane temperature estimates by [Law et al. \(2024\)](#) suggest a temperature of at least 30 K at the distance of PDS 70c.

When the planetary accretion luminosity dominates over the central brightness of the planet we have that the irradiation temperature is

$$T_{\text{irr}} = \left(\frac{L_{\text{acc}}}{\sigma 40\pi R^2} \right)^{1/4}, \quad (11)$$

if the disk receives 1/10 of the irradiation luminosity in the direction perpendicular to the disk (i.e. as in [Zhu et al. \(2018\)](#)).

The optically thick and thin regimes in τ_{mm} can be distinguished from Eq. 9. In the optically thick regime, since $T_{\text{eff}} \propto \dot{M}_p^{1/4}$ and $T_{\text{ext}} \propto \dot{M}_p^{1/4}$ this implies that $T_b \propto \dot{M}_p^{1/4}$ (except for large radii where $T_{\text{ext}} \sim T_{\text{floor}}$). This results in a mm-flux density depending solely on the accretion rate, $F_\nu \propto \dot{M}_p^{1/4}$.

In the optically thin regime $T_b \propto T_c \Sigma$. The mass column density Σ is calculated following [Zhu et al. \(2018\)](#), as the minimum between the equations

$$\Sigma = \frac{2^{7/5}}{3^{6/5}} \left(\frac{\sigma G M_p \dot{M}_p}{\alpha^4 \pi^3 \kappa_R R^3} \right)^{1/5} \left(\frac{\mu}{\mathfrak{R}} \right) \left[1 - \left(\frac{R_{\text{in}}}{R} \right)^{1/2} \right]^{3/5} \propto \left(\frac{\dot{M}_p^3}{\alpha^4} \right)^{1/5}, \quad (12)$$

and

$$\Sigma = \frac{\dot{M}_p \mu \Omega}{3\pi \alpha T_{\text{ext}}} \propto \left(\frac{\dot{M}_p^3}{\alpha^4} \right)^{1/4}, \quad (13)$$

where \mathfrak{R} is the ideal gas constant and μ is the mean molecular weight set as $\mu = 1$. And the mid-plane temperature is given by ([Zhu et al. 2018](#))

$$T_c = \left(\frac{9 G M_p \dot{M}_p \Sigma \kappa_R}{128 \pi \sigma R^3} \left[1 - \left(\frac{R_{\text{in}}}{R} \right)^{1/2} \right] + T_{\text{ext}}^4 \right)^{1/4}. \quad (14)$$

If we neglect the contribution of T_{ext} , that is for a purely viscously-heated disk, then we keep Σ from Eq. 12, and Eq. 14 yields

$$T_c \Sigma = \sqrt{\frac{G M_p}{\pi^2 R^3}} \frac{\dot{M}_p}{\alpha} \left(\frac{\mu}{\mathfrak{R}} \right)^{5/4} \left[1 - \left(\frac{R_{\text{in}}}{R} \right)^{1/2} \right]. \quad (15)$$

Finally from Eq. 8 if the disk becomes optically thin at a sufficient small radii, that is the case with $\tau_{\text{mm}} < 0.5$ of Eq. 9, T_b can be calculated using Eq. 15 since most of the contribution will come from larger radii (optically thin case).

The following simplifications can be made if the accretion rate is small enough. First, neglect the planetary accretion luminosity relative with the viscous heating mechanism with $T_{\text{ext}} \sim 0$. Second, approximate that the CPD is mostly optically thin by lowering the surface density $\Sigma \propto (\dot{M}_p^3 / \alpha^4)^{1/5}$. A CPD heated by viscous dissipation allows for a simplified model of the SED, with optically thin mm-emission that depends on a single parameter,

$$\gamma = \frac{\dot{M}_p / (M_{\text{Jup}} / \text{yr})}{\alpha}. \quad (16)$$

3.3. H I free-free component of the CPD

Another component of the SED from PDS 70c is free-free emission from the disk itself. This scenario is supported by mid-plane temperatures exceeding 10^4 K in the steady-state CPD models of [Zhu et al. \(2018\)](#). Also, the hydrogen recombination leading to the H α signal from PDS 70c ([Haffert et al. 2019](#)) implies that the radio signal is, at some level, partly due to H I free-free continuum emission.

Here we consider the H I free-free luminosity of the parametric disk models from [Zhu et al. \(2018\)](#). The surface density $\Sigma(R)$ (Eqs. 12 and 13), gives information on the gas density. Only the regions hot enough to ionise hydrogen ($T \gtrsim 10000 \text{ K}$) will contribute to the flux, and we neglect free electrons contributed by other elements.

Assuming that the gas follows a hydro-static and Gaussian vertical profile,

$$\rho(R, z) = \frac{\Sigma(R)}{\sqrt{2\pi} H(R)} \exp\left(-\frac{z^2}{2H(R)^2}\right), \quad (17)$$

with the scale height $H(R) = c_s/\Omega(R)$. We solve the radiative transfer equation with vertical stratification of the temperature (following [Hubeny 1990](#)),

$$T(z)^4 = \frac{3}{8} T_{\text{eff}}^4 \tau_R + T_{\text{ext}}^4, \quad (18)$$

where τ_R is the Rosseland mean optical depth at z . We can calculate the number density of electrons using the Saha equation

$$\frac{n(\text{H II})}{n(\text{H I})} = \frac{2Q_{\text{II}}}{n_e Q_{\text{I}}} \left(\frac{2\pi m_e k_B T}{h^2} \right)^{3/2} \exp\left(-\frac{\chi}{k_B T}\right), \quad (19)$$

where m_e is the electron mass, k_B is the Boltzmann constant, χ is the collisional ionisation potential of hydrogen (13.6 eV), h is the Planck constant and the partition function was calculated as

$$Q_{\text{I}} = \sum_{n=1}^3 2n^2 \exp\left(-\frac{\chi(1 - 1/n^2)}{k_B T}\right), \quad (20)$$

for neutral hydrogen, and $Q_{\text{II}} = 1$ for ionized hydrogen. The ionisation fraction of an initially neutral gas is given by $f = n_e/n_{\text{H}}$, where $n_{\text{H}} = \rho(R, z)/m_{\text{H}}$ (we assume the gas consists of hydrogen only). We can then solve for n_e ,

$$n_e(R, z) = \frac{Q_{\text{II}}}{Q_{\text{I}}} \left(\frac{2\pi m_e k_B T}{h^2} \right)^{3/2} \exp\left(-\frac{\chi}{k_B T}\right) \left(-1 + \sqrt{1 + 2n_{\text{H}} \frac{Q_{\text{I}}}{Q_{\text{II}}} \left(\frac{2\pi m_e k_B T}{h^2} \right)^{-3/2} \exp\left(-\frac{\chi}{k_B T}\right)} \right). \quad (21)$$

With the number density of electrons we calculate the emission measure (EM)

$$\text{EM}(R, z) = \int_z^\infty n_e(R, z) n_i(R, z) dz, \quad (22)$$

where n_i is number density of positive ions (for this initially neutral gas $n_i = n_e$). And the optical depth ([Wright & Barlow 1975](#); [Allen 1973](#), including stimulated emission),

$$\tau_v(R, z) = \int_z^\infty K_v(T) n_e(R, z) n_i(R, z) dz, \quad (23)$$

with

$$K_v(T) = \frac{4\pi}{3\sqrt{3}} \frac{Z^2 e^6}{h c m_e^2 v} \frac{g_v}{v^3} \left(1 - \exp\left(-\frac{h\nu}{k_B T}\right) \right) = \frac{3.692 \times 10^8}{\text{cm}^{-5} \text{K}^{-1/2} \text{Hz}^{-3}} \left(1 - \exp\left(-\frac{h\nu}{k_B T}\right) \right) Z^2 g_v T^{-1/2} v^{-3}, \quad (24)$$

where the electron velocity v was replaced by the mean velocity $\bar{v} = (\pi k T / 2 m_e)^{1/2}$, Z is the ionic charge (in this case $Z = 1$), e is the electron charge and c is the velocity of light in vacuum. The Gaunt factor, g_v , was approximated using the equation from [Oster \(1961\)](#)

$$g_v(T) = \ln \left(\left(\frac{2k_B T}{\gamma m_e} \right)^{3/2} \left(\frac{2m_e}{\gamma Z e^2 \omega} \right) \right) = \ln \left(4.955 \times 10^7 \left(\frac{\nu}{\text{Hz}} \right)^{-1} \right) + 1.5 \ln \left(\frac{T}{\text{K}} \right), \quad (25)$$

with $\gamma = e^{\gamma^*} \approx 1.781$ the exponential of Euler's constant γ^* and $\omega = 2\pi\nu$ the angular frequency. When $g_v(T) < 1$, we set $g_v(T) = 1$, which is the limit at higher frequencies.¹

Finally, we calculate the free-free emission from the CPD by integrating over the disk

$$F_\nu = \int_{R_{\text{in}}}^{R_{\text{out}}} \int_{-\infty}^{\infty} e^{-(\tau_v - \tau'_v)} B_\nu(T(z')) K_\nu(T(z')) n_e^2(R, z') dz' \frac{2\pi R}{d^2} dR, \quad (26)$$

where we have already replaced $n_i = n_e$, $B_\nu(T)$ is the Planck function, $\tau_v = \tau_v(R, z \rightarrow -\infty)$ and $\tau'_v = \tau_v(R, z')$ from Eq. 23. The distance to PDS 70 is d .

3.4. Uniform slab model

In parallel to the calculation of the free-free component from the analytic viscous disk model, we also implement a simpler treatment in order to inform on the emission measures and disk sizes that would match the observed SED. We use a pill-box model consisting of a uniform slab with a constant temperature and emission measure, and a cross-section of $A = \pi R_{\text{max}}^2$. The optical depth given by Eq. 23 reduces to

$$\tau_v^{\text{pill}} = K_\nu(T) \times \text{EM}, \quad (27)$$

then from Eq. 26, since T and EM are constants, we solve both integrals analytically using $R_{\text{in}} = 0$ and $R_{\text{out}} = R_{\text{max}}$ and obtain

$$F_\nu^{\text{pill}} = \pi B_\nu(T) \left(1 - e^{-\tau_v^{\text{pill}}} \right) \left(\frac{R_{\text{max}}}{d} \right)^2. \quad (28)$$

3.5. Magnetic disk

The previous models did not take into account the free electrons coming from metals, since the viscous disk models in consideration reach hydrogen-ionising temperatures. However, the very high effective viscosity in a strongly magnetised disk would result in lower peak temperatures, as in the parametric disk models from [Hasegawa et al. \(2021\)](#). Such ‘‘magnetic disk’’ models assume that the planet is undergoing magnetospheric accretion, which means that the inner region of the CPD has enough free electrons to couple the gas to the magnetic field of the planet.

We followed [Hasegawa et al. \(2021\)](#), with a magnetic field (B_p) described as a dipole

$$B_p = B_{\text{ps}} \left(\frac{R_p}{R} \right)^3, \quad (29)$$

where B_{ps} is the field strength at the surface of the planet. We use an alpha-viscosity (α_m) inspired by the results of ideal magneto-hydrodynamics (MHD) simulations of [Salvesen et al. \(2016\)](#),

$$\alpha_m = 11 \beta^{-0.53}, \quad (30)$$

where $\beta = \rho_o c_s^2 / (B_p^2 / 8\pi)$ and $\rho_o = \Sigma \Omega / (\sqrt{2\pi} c_s)$ is the mid-plane gas volume density.

Since the dusty disk model from Sec. 3.2 already has the disk surface density $\Sigma(R)$ and the temperature profile $T_c(R)$ for a given α and \dot{M}_p , we can solve Eq. 30 by imposing $\alpha = \alpha_m$ for a fixed B_{ps} and \dot{M}_p . Thus, the magnetic disk model has a variable viscous parameter $\alpha(R)$, with the rest of the physical conditions

¹ There is a typo in the formula for the Gaunt factor in [Beckert et al. \(2000, their Eq. 25\)](#). Here we use the constants from [Oster \(1961\)](#).

Table 5. The atomic number (Z), Abundance and collisional ionisation potential (χ_i) of the most relevant elements.

Element	Z	Abundance	χ_i (eV)
H	1	9.21×10^{-1}	13.60
He	2	7.84×10^{-2}	24.59
Na	11	1.60×10^{-6}	5.14
Mg	12	3.67×10^{-5}	7.65
K	19	9.87×10^{-8}	4.34

calculated analogously to Sec 3.2. However, these viscosity estimates neglect other sources of ionisation (i.e. interstellar UV and cosmic rays), and α values can be unrealistically low at large radii. We therefore imposed a lower limit $\alpha(R) > 10^{-5}$.

With the temperature and density profiles as a function of \dot{M}_p and B_{ps} , the next step was to consider the free electrons coming from the metals. For this we used the abundances and collisional ionisation potentials of the most relevant elements in the solar photosphere, shown in Table 5 (Asplund et al. 2009; Lide 2008; Keith & Wardle 2014).

We used these abundances and solved the Saha equation for each element, imposing the neutrality condition

$$n_e = \sum_i n_i, \quad (31)$$

where the sum runs over the 5 elements in consideration, and n_i is the number density of the i -ionised element. We assumed that the metals are not depleted into dust. However, solving this equation takes too long for an optimisation. We decided to use a simpler approach that takes advantage of the differences in abundance of each element. We assume that at a given temperature a single element contributes most of the free electrons. We solved the Saha equation separately, setting $n_e = n_i$ for each element, and used the abundances to determine which element provided most of the electrons at a given temperature. This allows for an approximation to the real number density of electrons without requiring an excessively long computing time.

Following Hasegawa et al. (2021), we take into account that the CPD is undergoing magnetospheric accretion. This means that the radius where the planetary magnetic field dominates over the ram pressure (called the truncation radius R_T) is larger than the radius where the disk has enough free electrons to couple the gas to the magnetic field. This condition is satisfied for $T \sim 1000$ K, which is the temperature threshold for K, and we used the condition $R_T > R(T_c = 1000 \text{ K})$ to ensure that the model is consistent (Hasegawa et al. 2021). Finally, we calculated the optical depth due to metal free-free using the electron number density on Eq. 23.

3.6. Negative hydrogen ion contribution

The optical/IR opacity of the sun and cooler stars is dominated by the negative hydrogen ion H^- (Wildt 1939), and it is worth exploring how it contributes to the CPD radio opacity. Because of its simple and highly polarised structure, the hydrogen atom can hold a second electron with a ionization potential of 0.7542 eV (Frolov 2015).

We include Wildt's photo-detachment, which is the bound-free mechanism,



where any photon with $\lambda < 16440 \text{ \AA}$ had sufficient energy to ionise the H^- . We also included Pannekoek's free-free mechanism (Pannekoek 1931),



which will contribute to the opacity specially into the longer wavelengths.

The presence of ionised metals is key to the abundance of H^- , since we need extra electrons to encounter neutral hydrogen, and H^- also draws free electrons from the medium. This means we have to solve Saha's equation again adding the H^- . We have its ionisation energy (0.7542 eV), partition function $Q_{H^-} \sim 1$, $Q_H \sim 2$ and a new neutrality condition

$$n_e + n_{H^-} = \sum_i n_i, \quad (34)$$

that follows from Eq. 31. The difference is that some of the free electrons from the ionised metals are now bound to the H^- .

Here again we simplify the solution of the Saha equation, by taking advantage of the different abundances of each element. In most of the cases, the abundance of H^- was negligible compared with the ions, and we solved Saha's equation as shown in Sec 3.5. We calculated the number density of H^- with the number density of electrons (n_e) obtained with metals only. In the case where the number density of H^- becomes significant (10% of the ions or more), the free electrons are less abundant in the medium. The number density of free electrons decreases drastically and we set $n_i = n_{H^-} = n_e = 0$.

Provided with the number density of electrons, we calculate the bound-free and free-free opacities of H^- following Gray (2022, their Chap. 8). The final total optical depth is,

$$\tau_{\nu}^{\text{tot}} = \tau_{\nu}^{\text{metals}} + \tau_{\nu}^{H^- \text{ bf}} + \tau_{\nu}^{H^- \text{ ff}}, \quad (35)$$

with $\tau_{\nu}^{\text{metals}}$ the optical depth calculated as Sec. 3.5, and $\tau_{\nu}^{H^- \text{ bf}}$ and $\tau_{\nu}^{H^- \text{ ff}}$ the bound-free and free-free optical depth of H^- respectively. The total flux then is calculated as

$$F_{\nu} = \int_{R_{\text{in}}}^{R_{\text{out}}} \int_0^{\tau_{\nu}} e^{-(\tau_{\nu} - \tau'_{\nu})} B_{\nu}(\tau'_{\nu}) d\tau'_{\nu} \frac{2\pi R}{d^2} dR, \quad (36)$$

where τ_{ν} is the τ_{ν}^{tot} calculated using Eq. 35.

3.7. Fitting the data

We first fit the nearly coeval data in Bands 3, 4, 7 and 9 using the dusty CPD model from Sec. 3.2, varying both parameters (α and \dot{M}_p). We observed that the accretion rate and viscosity parameters were degenerate, and therefore applied the simpler model that only depends on γ (Eq. 16). The best fit of both models is shown in Fig. 6, which poorly fits the data.

For the dusty disk model shown in Fig. 6, we observed that the bulk of the flux originates from the outer radius, where the mid-plane temperature is $T_c = T_{\text{ext}} \approx T_{\text{floor}} = 27 \text{ K}$. This indicates that the SED is highly dependent on the floor temperature, and our approximation using the single parameter γ was invalid (T_{ext} cannot be neglected). As shown in Fig. 7, if the floor temperature were lower (i.e. $T < 15 \text{ K}$), we could fit the data.

The addition of an optically thin and thick jet to the dusty disk model was performed. We fixed $\alpha = 10^{-2}$ and also vary the dust/gas ratio ζ , using uniform priors with $\log(\gamma)$ and $\log(\zeta)$ between -15 and 15. However, in both cases the contribution of

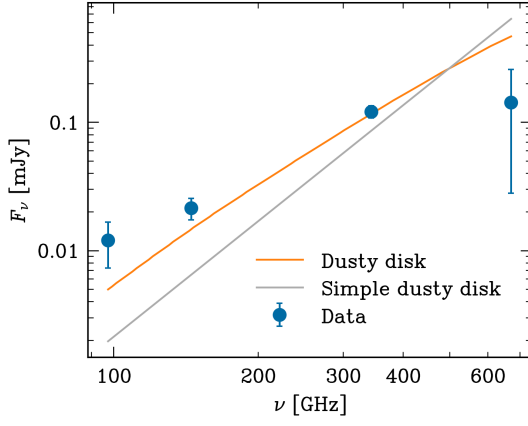


Fig. 6. Best fit for the data of Bands 3, 4, 7 and 9 using the dusty disk (Zhu et al. 2018) model and the simple dusty disk model (described in Sec. 3.2), are shown as the orange and light grey solid lines respectively. For the dusty disk, we obtain that the best fit parameters of the model are $\log(\dot{M}_p/(M_{\text{Jup}}/\text{yr})) = -9.05^{+0.5}_{-2.86}$ and $\log(\alpha) = -4.84^{+0.55}_{-2.96}$ at 1σ . The resulting spectral index is 2.35 and has a minimum reduced χ^2 of 6.50. For the simpler dusty disk model, we obtain that the best fit parameter is $\log(\gamma) = -3.15^{+0.04}_{-0.05}$. The resulting spectral index is 3 and has a minimum reduced χ^2 of 14.61. Here the reduced χ^2 is the χ^2 divided by the number of points (data) minus the number of degrees of freedom in the model.

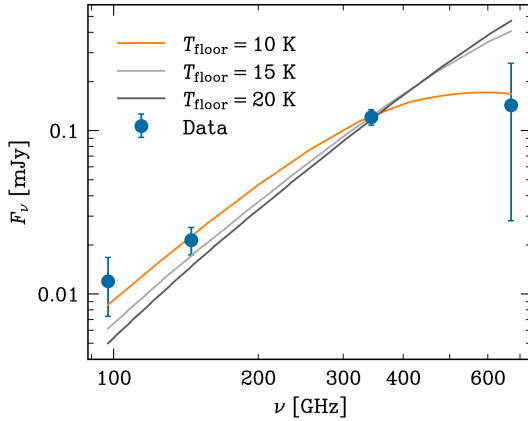


Fig. 7. Best fit for the data of Bands 3, 4, 7 and 9 for the dusty disk (Zhu et al. 2018) using different T_{floor} . In order the orange, light grey and grey solid lines corresponds to T_{floor} of 10, 15 and 20 K.

the jet after the fit was negligible and it just returned the dusty disk case without a jet.

We then turned to the new model that sums the free-free component (from Sec. 3.3) and the thermal dust emission from the disk. Since there is no certainty that the approximation made in Sec. 3.2 is valid (with the single parameter γ), we use the complete model proposed by Zhu et al. (2018). We consider two different models: (fixed α) we keep a fixed alpha value $\alpha = 10^{-2}$ and allow the accretion rate to vary, (fixed \dot{M}_p) we keep the accretion rate fixed at $\dot{M}_p = 10^{-6} M_{\text{Jup}} \text{ yr}^{-1}$ and allow the alpha value to vary. Fig. 8 shows the resulting best fits for each case. The models were able to produce spectral indices of $(\alpha_{97.5}^{145}, \alpha_{145}^{343.5}, \alpha_{343.5}^{671}) = (1.87, 1.85, 1.96)$ and $(\alpha_{97.5}^{145}, \alpha_{145}^{343.5}, \alpha_{343.5}^{671}) = (2.02, 1.93, 1.83)$ respectively, which are more consistent with Table 4 for Bands 3 to 7. However, these models only fit the data points for Bands 3, 4 and 7 but do not ac-

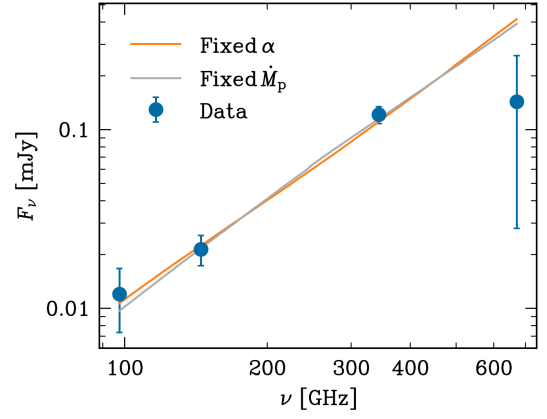


Fig. 8. Best fits to the data from Bands 3, 4, 7 and 9 using two free-free emission models (sum the dusty disk component from Sec. 3.2 and the free-free component from Sec. 3.3). The first has a fixed $\alpha = 10^{-2}$, shown as the solid orange line and has a minimum reduced χ^2 of 3.15. We obtain that the best fit parameters of this model are $\log(\dot{M}_p/(M_{\text{Jup}}/\text{yr})) = -3.68^{+0.05}_{-0.07}$ at 1σ , with a strict upper limit on the dust-to-gas ratio of $\log(\zeta) = -4.95$. The second has a fixed $\dot{M}_p = 10^{-6} M_{\text{Jup}} \text{ yr}^{-1}$ as the solid light grey line and has a minimum reduced χ^2 of 2.54. We obtain that the best fit parameters for this model are $\log(\alpha) = -6.48^{+0.09}_{-0.06}$ at 1σ , with a strict upper limit on the dust-to-gas ratio of $\log(\zeta) = -7.20$.

count for the non-detection in Band 9 with a flux F_{671} of $413 \mu\text{Jy}$ and $389 \mu\text{Jy}$ in each case.

In the model with fixed α we derive a well-constrained mass accretion rate, and vice versa. However, the results also indicate that free-free emission is the dominant component of the CPD signal. The inferred upper limits on the dust-to-gas ratio are $10^{-4.95}$ and $10^{-7.20}$ for the models with fixed α and fixed \dot{M}_p respectively. This suggests a strongly dust-depleted environment, which could point to reduced dust transport into the CPD, with larger grains being trapped in a pressure bump outside the planet's orbit (e.g. Zhu et al. 2012). Weber et al. (2018) showed that in the presence of viscosity, even with strong gap-opening planetary torques, there is a flow of gas and micron-sized grains through the planet-induced gap, while grains larger than a certain size are filtered out at the gap edge. In contrast, a study more focused on dust transport to the CPD by Szulágyi et al. (2022) reported a contradictory result: the planet's gravitational perturbation elevates millimeter-sized particles from the mid-plane and induces a vertical accretion flow from the circumstellar disk toward the CPD. Since Weber et al. (2018) considered a two-dimensional case over long evolutionary time-scales – leaving the planet sufficient time to clear its orbit – whereas Szulágyi et al. (2022) conducted three-dimensional simulations evolved for only 200 orbits, it remains an open question how dust filtration and transport operate in more evolved, three-dimensional cases.

The model with a fixed $\alpha = 10^{-2}$ requires very high accretion rates, $\dot{M}_p \sim 10^{-3.7} M_{\text{Jup}} \text{ yr}^{-1}$. However, by reducing the viscosity parameter, for example, to $\alpha = 10^{-3}$, the flux ends up being overestimated by more than a factor of two. This means that reducing the viscosity parameter would require a lower accretion rate to fit the data. Using the same example, for $\alpha = 10^{-3}$ the accretion rate that fits the data is $\dot{M}_p \sim 10^{-4.2} M_{\text{Jup}} \text{ yr}^{-1}$.

The properties of the disk are listed in Figs. 9 and 10 for the case with fixed α and fixed \dot{M}_p respectively. At small radii ($R \lesssim 0.02 \text{ au}$) the fraction of ionisation is $f \sim 1$, and the resulting emission measures are extremely large ($\text{EM} \sim 10^{26-31} \text{ cm}^{-6} \text{ pc}$).

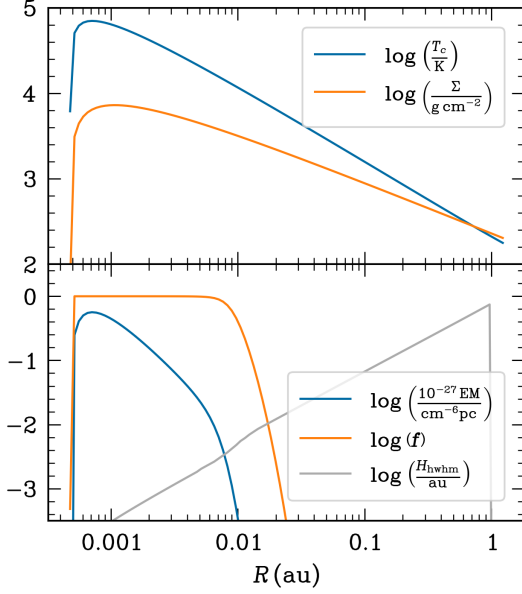


Fig. 9. Physical conditions including free-free in the best-fit CPD model with α fixed. T_c is the mid-plane temperature calculated as Eq. 14, $\Sigma(R)$ is the surface density, EM is the emission measure, f is the ionisation fraction in the mid-plane and H_{hwhm} is the height at which the density of free electrons is half the density of free electrons in the mid-plane (half-width at half-maximum).

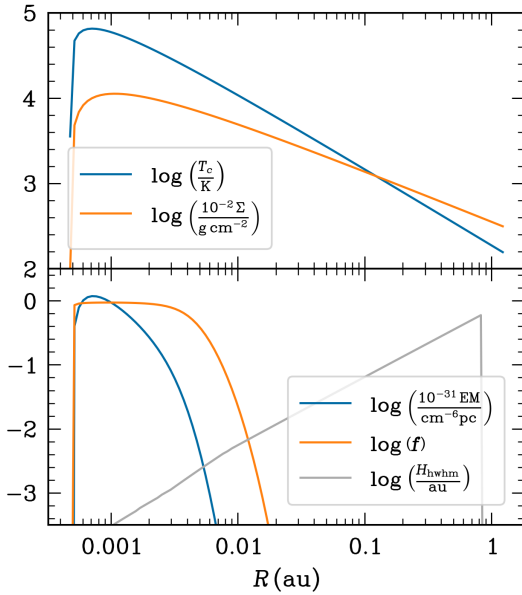


Fig. 10. Physical conditions in the best-fit CPD model with \dot{M}_p fixed. Annotations follow from Fig. 9.

The profile for the surface density (Σ) is in the viscous-disk regime (small T_{ext}) and in the case with fixed \dot{M}_p and small α (i.e. $\alpha \sim 10^{-6}$), Σ is two orders of magnitude higher than for large values of α (i.e. $\alpha \sim 0.01$). Another outstanding feature of the physical conditions in these analytical viscously accreting CPDs is the occurrence of extremely hot inner disks, for any $\alpha < 0.01$. Such hydrogen-ionising temperatures are counter-intuitive for a CPD.

For the uniform slab model we fixed a temperature of 10^3 K and 10^4 K and choose uniform priors for $\log(R_{\text{max}}/\text{au})$ and

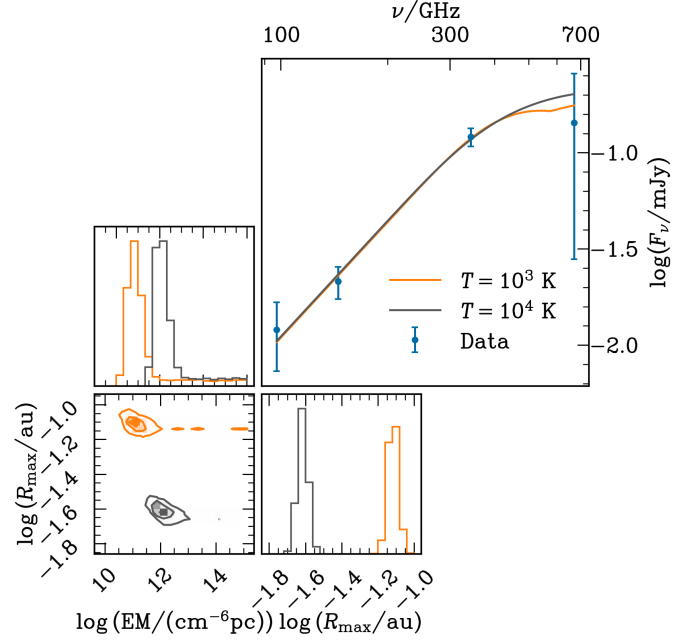


Fig. 11. Best fit to the data from Bands 3, 4, 7 and 9 using the uniform slab model described in Sec. 3.4. On the upper right panel, the solid orange line corresponds to the case $T = 10^3$ K, has a minimum reduced χ^2 of 0.18 and a p-value of 83%. We obtain that the best fit parameters of this model are $\log(\text{EM}/(\text{cm}^{-6} \text{ pc})) = 11.08^{+0.53}_{-0.19}$ and $\log(R_{\text{max}}/\text{au}) = -1.11^{+0.03}_{-0.06}$. The solid light grey line corresponds to the case $T = 10^4$ K, has a minimum reduced χ^2 of 0.33 and a p-value of 72%. We obtain that the best fit parameters of this model are $\log(\text{EM}/(\text{cm}^{-6} \text{ pc})) = 12.00^{+0.42}_{-0.18}$ and $\log(R_{\text{max}}/\text{au}) = -1.61^{+0.02}_{-0.04}$. The bottom left panel shows the corner plots obtained for each model. The orange and grey posteriors also corresponds to the cases of $T = 10^3$ K and $T = 10^4$ K respectively.

$\log(\text{EM}/(\text{cm}^{-6} \text{ pc}))$ (with very wide boundaries). The resulting best fits are shown in Fig. 11. Now we could produce spectral indices of $(\alpha_{97.5}^{145}, \alpha_{145}^{343.5}, \alpha_{343.5}^{671}) = (2.00, 1.91, 0.59)$ and $(\alpha_{97.5}^{145}, \alpha_{145}^{343.5}, \alpha_{343.5}^{671}) = (2.00, 1.88, 0.81)$ respectively, which are more in line with Table 4 even for Band 9.

We notice that the values for the EM are smaller compared with the parametric model of Zhu et al. (2018), having the best fit $\text{EM} = 1.19 \times 10^{11} \text{ cm}^{-6} \text{ pc}$ and $\text{EM} = 1.04 \times 10^{12} \text{ cm}^{-6} \text{ pc}$ for each case. On the other hand, the radius of the pill seems to match the order of magnitude of the radius where we start having less ionisation fraction in Figs. 9 and 10 having the best fit size of $R_{\text{max}} = 0.078 \text{ au}$ and $R_{\text{max}} = 0.025 \text{ au}$ for the pill in each case.

For the magnetic disk, we chose uniform priors for $\log(B_{\text{ps}}/\text{G})$ between -4 and 4 and $\log(\dot{M}_p/(M_{\text{Jup}}/\text{yr}))$ between -10 and -2. We also add a penalty in the log likelihood for the magnetospheric accretion criterion by subtracting the quantity $x = 10 \times \frac{|R_T - R(T_c = 1000 \text{ K})|}{R(T_c = 1000 \text{ K})}$ for the cases where $R_T < R(T_c = 1000 \text{ K})$. The resulting best fit is shown in Fig. 12. Now we could produce spectral indices of $(\alpha_{97.5}^{145}, \alpha_{145}^{343.5}, \alpha_{343.5}^{671}) = (1.85, 1.71, 1.72)$ that could marginally fit the data, and overestimate Band 9 with a flux F_{671} of $339 \mu\text{Jy}$.

From Fig. 13 we can see that the model satisfies the magnetospheric accretion criterion ($R_T > R(T_c = 1000 \text{ K})$). The radius of the peak EM, with $\text{EM} \sim 10^{11.5} \text{ cm}^{-6} \text{ pc}$, is $R \sim 0.02 \text{ au}$, and both EM and R approximate those required by the uniform slab model. The size of the magnetic disk model is smaller than the

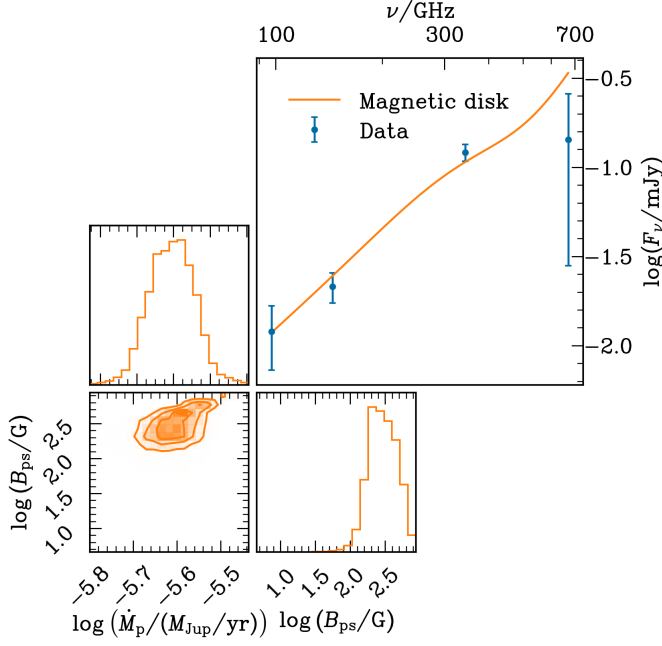


Fig. 12. Results using the magnetic disk model described in Sec. 3.5, this takes into account the free-free from metals and H^- and the bound-free from H^- as described in Sec. 3.6. On the upper right we have the best fit for the data of Bands 3, 4, 7 and 9 represented with their error bars using the fluxes of Table 3. The modelled flux is represented by the solid line, obtaining a partially thick free-free emission with a spectral index of 1.74. On the bottom left we have the corner plot with the best fit parameters $\log(\dot{M}_p/(M_{Jup}/yr)) = -5.54^{+0.02}_{-0.13}$ and $B_{ps} = 613^{+95}_{-409}$ G at 1σ . The minimum reduced χ^2 is 2.32.

1/10 the Hill radius, which is reminiscent of the upper limit to the extension of the sub-mm signal observed in SR 12c (Wu et al. 2022).

Because of the residual ionisation stemming from collisional ionisation of metals, part of the atomic phase of the CPD can be seen as an atomic plasma. This state of matter is characterised by temperatures $T \sim 1000 - 2000$ K. The free electrons released by the metals interact with both neutral hydrogen and ionised metals, and thus originate the radio signal.

Atomic plasma radiation in the magnetic disk model can marginally fit the data. However, an optically thick spectrum persists at higher frequencies and the drop in Band 9 cannot be reproduced. This is because, even though the magnetic disk reaches the necessary emission measures for free-free emission from ionised metals, H^- free-free also contributes to the total optical depth. In Fig. 14 the optical depth of metals behaves exactly as we would like it to, going from optically thick to thin from 97.5 GHz to ~ 500 GHz. However, the optical depth of H^- begins to dominate above 500 GHz, and the total optical depth remains $\tau \sim 1$ without reaching the optically thin regime.

The atomic plasma model, however, depends heavily on the accuracy of the extrapolation from the H^- opacities, specially the free-free opacity that dominates in the sub-mm continuum. Gray (2022) was inspired by works that calculated opacities up to $10\mu m$ and in a range of temperatures from 2500 to 10000 K. This is very important here, since we are calculating the opacity in mm wavelengths, and in a cold disk, where the majority of the flux comes from temperatures $T \approx 1000 - 2000$ K.

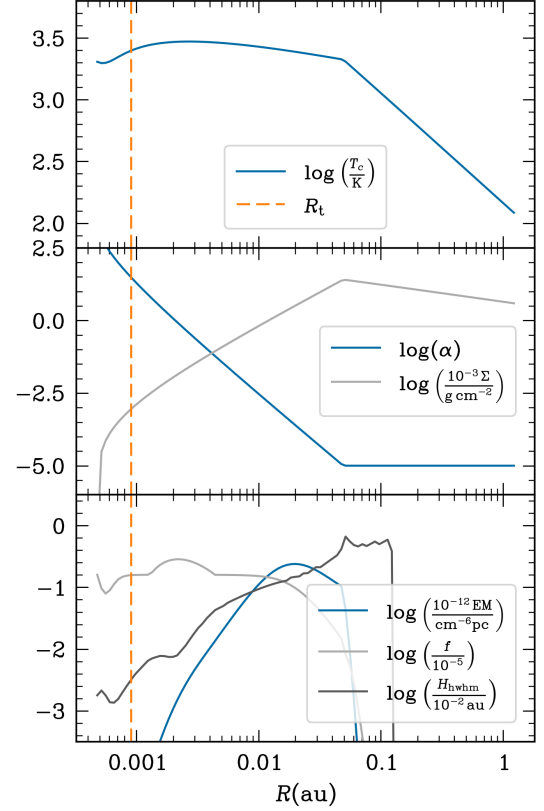


Fig. 13. Physical conditions including metal free-free emission in the best-fit MHD model. α is the viscosity parameter, T_c is the mid-plane temperature calculated according to Eq. 14, $\Sigma(R)$ is the surface density, EM is the emission measure, f is the ionisation fraction in the mid-plane and H_{hwhm} is the height at which the density of free electrons is half the density of free electrons in the mid-plane (half-width at half-maximum). The vertical dashed red line is the truncation radius $R_t = 1.89R_{Jup}$ and the disk total mass is $3.07M_{Jup}$.

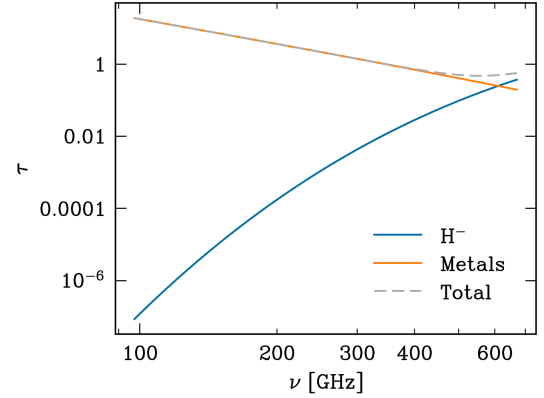


Fig. 14. The optical depth of H^- (including free-free and bound-free) and metals, in the annulus that makes the greatest contribution to the flux for the magnetic disk model (Sec. 3.5). The blue and orange solid lines corresponds to the optical depth by H^- and metals respectively, the dashed line is the total optical depth.

4. Discussion

4.1. Which models fit the data?

The best fits obtained for the dusty disk model, shown in Fig. 6, have spectral indices of $\alpha > 2.35$ and do not fit the data, even be-

tween Bands 3 and 7. Adding a jet, either optically thin or thick, does not change this result. However, we observe that the bulk of the flux stems from the outer regions of the disk. If the temperature is low enough ($T_{\text{floor}} < 15$), then a dusty disk can fit the data, as shown in Fig. 7. This can be understood from the Wien displacement law, which states that at such low temperatures, the turnover of the blackbody spectrum is close to the Band 9 frequency. However, these low temperatures are unlikely, as mentioned in Sec. 3.2. Band 9 shows a lower temperature limit of 21 K at 34 au, and the presence of CO in the PDS 70 cavity suggests temperatures of at least 30 K (Law et al. 2024). Therefore, we conclude that it is not possible to fit the observed SED using only a dusty disk model with the current derivations of T_{floor} .

If viscous heating is efficient and reaches H-ionising temperatures, our best fit with H I free-free from the H II disk reaches $\text{EM} \sim 10^{26-31} \text{ cm}^{-6} \text{ pc}$ (see Figs. 9 and 10), which seems overwhelming and would approximate the radio spectrum of an early-type star. This results in an optically thick SED which overshoots the flux density in Band 9.

Uniform slab model can inform about the parameters needed to produce the Band 9 drop, with an emission measure of $\text{EM} \sim 10^{11-12} \text{ cm}^{-6} \text{ pc}$, temperatures of $T \sim 10^3 - 10^4 \text{ K}$ and sizes of $\sim 0.1 \text{ au}$. Comparing these emission measures and temperatures with those from the H II disk (see the implicit dependence of EM and T in Figs. 9 and 10), we see that such emission measures in an H II CPD would require low ionisation fractions, and hence fine-tuning of the temperature. Since $f(T)$ is extremely sensitive to T , we conclude that the CPD is probably not hot enough to ionise hydrogen, as, unless the temperature field is “just right”, hydrogen-ionisation results in huge EM and a very optically thick SED (and inconsistent, at 2.6σ , with the non-detection in Band 9).

Finally, if the planet has a significant magnetic field ($B_{\text{ps}} > 200 \text{ G}$), magnetospheric accretion occurs, the temperature drops to $\sim 10^3 \text{ K}$ and the signal stems from free-free emission from ionised metals at lower frequencies ($\nu \lesssim 500 \text{ GHz}$) and from H^- at higher frequencies ($\nu > 500 \text{ GHz}$). This atomic plasma radiation model maintains a partially optically thick SED above 500 GHz and also overshoots Band 9.

4.2. Surface shock on the CPD

The small emission measures from the uniform-slab models are reminiscent of shock models, as studied by Aoyama et al. (2018) and Aoyama et al. (2020) for the CPD surface shock and Aoyama et al. (2020) for the photospheric shock. These shocks arise from the supersonic, nearly vertical gas flows that collide with the CPD or planetary surfaces, as predicted in detailed hydro-dynamical simulations Tanigawa et al. (2012); Szulágyi & Ercolano (2020). The strong shock heats the gas and results in a thin, non-equilibrium layer of ionised hydrogen.

Because of the high temperatures ($T \gtrsim 10^4 \text{ K}$) in the post-shock gas, we can neglect contributions from H^- to the net opacity. The bulk of the mass is at a relative constant temperature of $\sim 10^4 \text{ K}$. Since the most emission originates from the region with $T \sim 10^4 \text{ K}$, we refer to 10^4 K as the effective temperature for free-free emission (Aoyama et al. 2018, 2020). As seen in the uniform slab model of Sec. 3.4 for temperatures of 10^4 K , an effective radius of $\sim 52^{+5}_{-5} R_{\text{Jup}}$ is required to fit the SED. This indicates that the flux in the radio should come from shocks on the CPD and neither from the photosphere nor accretion funnels (whose sizes are $\sim 2 R_{\text{Jup}}$).

To firmly rule out photospheric shocks and accretion funnels, we estimate the temperature and emission measure needed for a

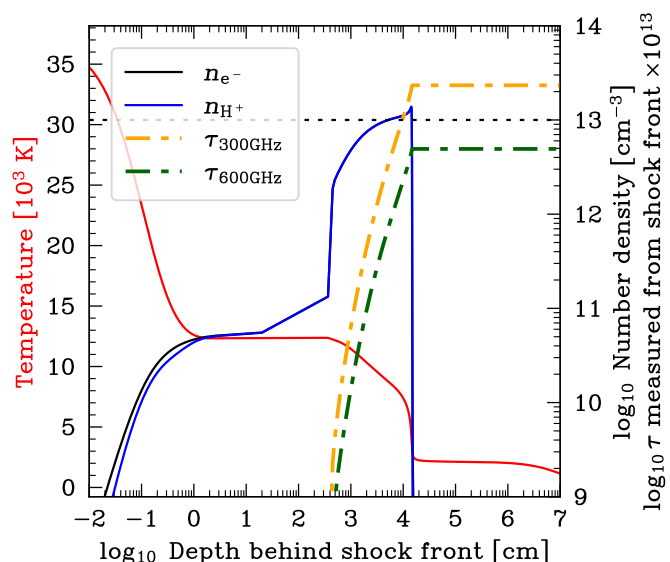


Fig. 15. Physical conditions of the post shock region for $v_0 = 30 \text{ km s}^{-1}$ and $n_0 = 10^{15} \text{ cm}^{-3}$. The temperature, free electron local density (n_{e^-}) and H II local density (n_{H^+}) are the red, black and blue solid lines respectively. The optical depths at 300 and 600 GHz ($\tau_{300 \text{ GHz}}$ and $\tau_{600 \text{ GHz}}$) are the green and yellow dashed lines where the dotted black line corresponds to $\tau = 1$.

fixed size of $R_{\text{max}} = 2 R_{\text{Jup}}$ in the uniform slab model. The best fit parameters are $\log(T/\text{K}) = 6.83^{+0.04}_{-0.10}$ and $\log(\text{EM}/(\text{cm}^{-6} \text{ pc})) = 15.75^{+10.11}_{-0.14}$. Such temperatures are only achieved in the post-shock region of an object $> 200 M_{\text{Jup}}$ with a $2 R_{\text{Jup}}$ radius, which is out of planetary regime. High temperatures, in excess of $\sim 10^6 \text{ K}$, also quench $\text{H}\alpha$ radiation as recombination becomes less probable. Therefore a photospheric shock, or free-free emission from the accretion funnels, cannot be the source of the radio signal as such shocks would require excessively large temperatures, given the free-fall velocities in the planetary regime. Note that part of the $\text{H}\alpha$ signal from PDS 70c could still stem from a $\sim 10^4$ shock on the planetary surface, even if such shock does account for the radio signal.

To confirm that the post-shock emission on the CPD surface can indeed reproduce the observed radio emission, we performed two simulations of shock-heated gas following Aoyama et al. (2018), whose results are shown in Figs. 15 and 16. These correspond to pre-shock velocities and neutral hydrogen number densities of $(v_0, n_0) = (30 \text{ km s}^{-1}, 10^{15} \text{ cm}^{-3})$ and $(50 \text{ km s}^{-1}, 10^{12} \text{ cm}^{-3})$ respectively. In both cases, the emission at 300 GHz is optically thick ($\tau > 1$) but turns-over into an optically thin spectrum at 600 GHz ($\tau \sim$ a few times 0.1). This is also the case for the SED of PDS 70c obtained with the uniform slab model, with a best fit of $\tau_{300 \text{ GHz}} \approx 3$ and $\tau_{600 \text{ GHz}} \approx 0.6$.

In these simulations, the optical-depth weighted temperature are ~ 7000 and $\sim 7500 \text{ K}$, for $v_0 = 30 \text{ km s}^{-1}$ and $v_0 = 50 \text{ km s}^{-1}$, respectively. A uniform slab at 7000 K requires a radius $R_{\text{max}} = 62 R_{\text{Jup}}$, that is in between the values obtained for the uniform slab models at 10^3 K and 10^4 K shown in Fig 11. We can estimate the planetary mass required to achieve a pre-shock velocity of $v_0 > 30 \text{ km s}^{-1}$ at $62 R_{\text{Jup}}$, by assuming v_0 is the free-fall velocity,

$$v_0 = \sqrt{\frac{2GM_{\text{p}}}{r}}. \quad (37)$$

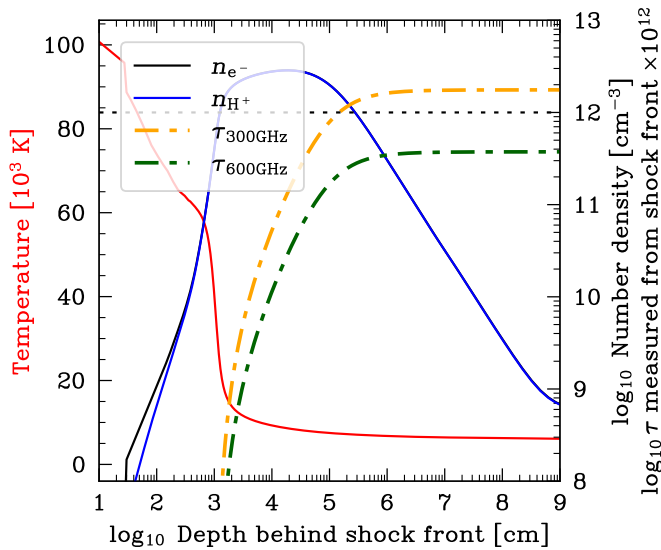


Fig. 16. Physical conditions of the post shock region for $v_0 = 50 \text{ km s}^{-1}$ and $n_0 = 10^{12} \text{ cc}^{-1}$. Annotations follow from Fig. 15.

A minimum planetary mass of $15.7 M_{\text{Jup}}$ is required, which is $2.1 M_{\text{Jup}}$ above the 2σ -upper limit of $13.6 M_{\text{Jup}}$ estimated for the dynamical mass of PDS70c (Trevascus et al. 2025). This minimum planetary mass could be reduced by considering the increasing v_0 at smaller radii, and its resulting radio flux, but this is beyond the scope of this work.

Using a mean molecular weight $\mu = 1.35$, $v_0 = 30 \text{ km s}^{-1}$ and $n_0 = 10^{15} \text{ cc}^{-1}$ imply a mass flux $\mu m_{\text{H}} \times n_0 \times v_0 = 6.75 \times 10^{-3} \text{ cm}^{-2} \text{ s}^{-1} \text{ g}$. If this flux is spatially constant and falls both sides of a circular slab with a radius of $62 R_{\text{Jup}}$, the mass influx rate within this area is $0.1 M_{\text{Jup}} \text{ yr}^{-1}$. For $v_0 = 50 \text{ km s}^{-1}$ and $n_0 = 10^{12} \text{ cc}^{-1}$, the crude estimate of the mass influx rate is instead $2 \times 10^{-4} M_{\text{Jup}} \text{ yr}^{-1}$, for simplicity using the same effective radius of $62 R_{\text{Jup}}$. These rough estimates of the accretion rate may seem extremely high. However, not all of the mass falling on the CPD is necessarily accreted by the planet because of equatorial deceleration and recycling of the CPD mass along the planetary wakes (Szulágyi et al. 2016; Batygin 2018).

Moreover, while we assumed a constant mass flux across the entire CPD, as in Aoyama et al. (2018), a concentration of mass flux toward the inner region could significantly lower the mass-accretion-rate estimate while preserving the radio flux. The larger v_0 and radio intensity at smaller radii could produce the same radio flux with a smaller mass accretion rate. The radial distribution of CPD mass-loading is, however, an open question, with some studies favouring the outer regions of CPDs (Tani-gawa et al. 2012; Marleau et al. 2024).

If the observed radio signal from PDS 70c is entirely due to H I free-free emission from the CPD surface shock, the emission from the CPD itself must be faint. This places an upper limit to the planetary accretion rate. Using the magnetic disk model from Sec. 3.5 with the best fit value of $B_{\text{ps}} = 613 \text{ G}$, we obtain an upper limit of $\log(\dot{M}_{\text{p}}/(M_{\text{Jup}}/\text{yr})) < -5.59$ using the 3σ flux limit in Band 7. In the case of a smaller magnetic field (for example $B_{\text{ps}} = 200 \text{ G}$), the upper limit for the accretion rate diminishes to $\log(\dot{M}_{\text{p}}/(M_{\text{Jup}}/\text{yr})) < -5.94$.

The non-detection of PDS 70b can be understood in the context of the CPD-surface shock if PDS 70b is less massive than PDS 70c (e.g. Trevascus et al. 2025). In this case, PDS 70b

would have the same v_0 at a smaller radii. As an illustration, for a $3 M_{\text{Jup}}$ planet, the pre-shock velocity $v_0 = 30 \text{ km s}^{-1}$ is obtained at $R_{\text{shock,b}} = 12 R_{\text{Jup}}$. This means that the radii for the shocked region where free-free emission arises is smaller and consequently the total flux decreases. As a rough approximation, the radio flux from PDS 70b would be lower than PDS 70c by a factor correspond to the ratio of the shocked surface area, or $\sim (R_{\text{max}}/R_{\text{shock,b}}) \sim (62/12)^2 \sim 30$.

5. Conclusion

We report on new ALMA observations of PDS 70, focussing on the point-source signal coincident with PDS 70c, with new detections in Bands 4 and 7, and a marginal detection in Band 3. The spectrum across Bands 3, 4 and 7 is consistent with optically thick emission, with $\alpha = 2.0 \pm 0.2$. However, a non-detection in Band 9 breaks this trend, with a flux density lower than an optically thick extrapolation of lower frequencies by at least 2.6σ . The Band 7 signal from PDS 70c appears to be constant within 10% rms, from May to Nov. 2023. Since the multi-frequency measurements are coeval within two months, we assume that the SED collected here is constant.

The non-detection in Band 9 is particularly surprising, given the model predictions for bright signal at short sub-mm wavelengths, and suggest a very dust poor disk, whose radio signal stems from partially thick free-free radiation. We interpret the observed SED in an adaptation of parametric CPD models, including the free-free emission from the disk itself.

A purely dusty disk cannot reproduce the SED of PDS 70c, even with the inclusion of free-free radiation from a jet. However, the H I free-free continuum from the CPD yields an optically thick SED, and marginally accounts for the data (within 3σ of Band 9). This free-free signal is intrinsic to the CPD and a product of the high temperatures reached by viscous heating in these analytic CPD models. Such an H II disk is at odds with the atomic or molecular environments expected in the context of planetary accretion.

Given an optically thick free-free spectrum, any steeper component is negligible, and the dust-to-gas mass ratio ζ must be very low, $\log(\zeta) < -4.95$. Such a dust-deprived environment could be the result of strong dust filtering inside the planet-induced gap.

Uniform slab models indicate the need for lower emission measures than obtained in constant-viscosity CPDs to account for the turn-over to partially thin free-free emission above Band 7 (see Fig. 11). The free-free signal would then stem from an atomic plasma, with residual ionisation from metals. The required emission measures and temperatures, of $T \sim 2000 \text{ K}$, are naturally produced in a magnetic disk models where large disk viscosity (up to $\alpha \sim 0.1$) results from a strong magnetic field.

Magnetic disk models result in similar radio SEDs as for the H II disk, but without reaching H-ionising temperatures, and with comparatively moderate emission measures ($\text{EM} \sim 10^{11.5} \text{ cm}^{-6} \text{ pc}$). However, because of the opacity of H⁻ free-free, an optically thick SED persists despite the lower emission measures, and still overshoots the Band 9 flux density.

The CPD surface shock model is the closest to the uniform slab requirements, and is therefore the only viable interpretation of the observed SED, including the Band 9 drop. Such surface shock requires inefficient planetary accretion with a strong mass flux onto the CPD, and correspondingly strong equatorial mass loss.

The radio SED of PDS 70c rules out a planetary surface shock, or accretion funnels, as the source of the signal. Such

small emitting regions would require temperatures in excess of 10^6 K to reach the observed flux densities, which cannot be produced in shock models in the planetary mass regime.

Acknowledgements. We thank the referee for constructive comments. O.D., S.C., M.C. and P.W. acknowledge support from Agencia Nacional de Investigación y Desarrollo de Chile (ANID) given by FONDECYT Regular grants 1211496, ANID MAGISTER NACIONAL BECAS CHILE/2025-22250525, ANID PFCHA/DOCTORADO BECAS CHILE/2018-72190574, ANID project Data Observatory Foundation DO210001, FONDECYT post-doctoral grant 3220399 and Millennium Science Initiative Program Center Code NCN2024_001, FONDECYT grant 3220399 and ANID – Millennium Science Initiative Program – Center Code NCN2024_001. The work of OC was supported by the Czech Science Foundation (grant 21-23067M), the Charles University Research Centre program (No. UNCE/24/SCI/005), and the Ministry of Education, Youth and Sports of the Czech Republic through the e-INFRA CZ (ID:90254). This paper makes use of the following ALMA data: ADS/JAO.ALMA#2022.1.00592.S, #2022.1.01477.S, 2022.1.00893.S. ALMA is a partnership of ESO (representing its member states), NSF (USA) and NINS (Japan), together with NRC (Canada), MOST and ASIAA (Taiwan), and KASI (Republic of Korea), in cooperation with the Republic of Chile. The Joint ALMA Observatory is operated by ESO, AUI/NRAO and NAOJ.

References

- Allen, C. W. 1973, *Astrophysical quantities* (London: University of London, Athlone Press)
- Andrews, S. M., Wilner, D. J., Hughes, A. M., et al. 2012, *ApJ*, 744, 162
- Anglada, G., Rodríguez, L. F., & Carrasco-González, C. 2018, *A&A Rev.*, 26, 3
- Aoyama, Y., Ikoma, M., & Tanigawa, T. 2018, *ApJ*, 866, 84
- Aoyama, Y., Marleau, G.-D., Mordasini, C., & Ikoma, M. 2020, *arXiv e-prints*, arXiv:2011.06608
- Asplund, M., Grevesse, N., Sauval, A. J., & Scott, P. 2009, *ARA&A*, 47, 481
- Batygin, K. 2018, *AJ*, 155, 178
- Beckert, T., Duschl, W. J., & Mezger, P. G. 2000, *A&A*, 356, 1149
- Benisty, M., Bae, J., Facchini, S., et al. 2021, *ApJ*, 916, L2
- Cárcamo, M., Román, P. E., Casassus, S., Moral, V., & Rannou, F. R. 2018, *Astronomy and Computing*, 22, 16
- Carrasco-González, C., Henning, T., Chandler, C. J., et al. 2016, *ApJ*, 821, L16
- CASA Team, Bean, B., Bhatnagar, S., et al. 2022, *PASP*, 134, 114501
- Casassus, S. & Cárcamo, M. 2022, *MNRAS*, 513, 5790
- Casassus, S., Cieza, L., Cárcamo, M., et al. 2023, *MNRAS*, 526, 1545
- Christiaens, V., Samland, M., Henning, T., et al. 2024, *A&A*, 685, L1
- Doi, K., Kataoka, A., Liu, H. B., et al. 2024, *ApJ*, 974, L25
- Fasano, D., Benisty, M., Curone, P., et al. 2025, *A&A*, 699, A373
- Frolov, A. M. 2015, *European Physical Journal D*, 69, 132
- Gaia Collaboration, Vallenari, A., Brown, A. G. A., et al. 2023, *A&A*, 674, A1
- Gray, D. F. 2022, *The observation and analysis of stellar photospheres* (Cambridge: Cambridge University Press)
- Haffert, S. Y., Bohn, A. J., de Boer, J., et al. 2019, *Nature Astronomy*, 3, 749
- Hammond, I., Christiaens, V., Price, D. J., et al. 2025, *MNRAS*, 539, 1613
- Hartmann, L. 1998, *Accretion Processes in Star Formation* (New York : Cambridge University Press)
- Hasegawa, Y., Kanagawa, K. D., & Turner, N. J. 2021, *ApJ*, 923, 27
- Hashimoto, J., Aoyama, Y., Konishi, M., et al. 2020, *AJ*, 159, 222
- Hubeny, I. 1990, *ApJ*, 351, 632
- Isella, A., Benisty, M., Teague, R., et al. 2019, *ApJ*, 879, L25
- Keith, S. L. & Wardle, M. 2014, *MNRAS*, 440, 89
- Kepler, M., Benisty, M., Müller, A., et al. 2018, *A&A*, 617, A44
- Lange, J. U. 2023, *MNRAS*, 525, 3181
- Law, C. J., Benisty, M., Facchini, S., et al. 2024, *ApJ*, 964, 190
- Lide, D. R. 2008, *CRC Handbook of chemistry and physics: a ready-reference book of chemical and physical data* (Boca Raton, FL: CRC Press)
- Liu, H. B., Casassus, S., Dong, R., et al. 2024, *ApJ*, 972, 163
- Marleau, G.-D., Aoyama, Y., Hashimoto, J., & Zhou, Y. 2024, *ApJ*, 964, 70
- Oster, L. 1961, *Reviews of Modern Physics*, 33, 525
- Pannekoek, A. 1931, *MNRAS*, 91, 519
- Quillen, A. C. & Trilling, D. E. 1998, *ApJ*, 508, 707
- Salvesen, G., Simon, J. B., Armitage, P. J., & Begelman, M. C. 2016, *MNRAS*, 457, 857
- Samland, M., Mollière, P., Bonnefoy, M., et al. 2017, *A&A*, 603, A57
- Shibaike, Y., Hashimoto, J., Dong, R., et al. 2025, *ApJ*, 979, 24
- Szulágyi, J., Binkert, F., & Surville, C. 2022, *ApJ*, 924, 1
- Szulágyi, J. & Ercolano, B. 2020, *ApJ*, 902, 126
- Szulágyi, J., Masset, F., Lega, E., et al. 2016, *MNRAS*, 460, 2853
- Szulágyi, J., Plas, G. v. d., Meyer, M. R., et al. 2018, *MNRAS*, 473, 3573
- Tanigawa, T., Ohtsuki, K., & Machida, M. N. 2012, *ApJ*, 747, 47
- Trevascus, D., Blunt, S., Christiaens, V., et al. 2025, *A&A*, 698, A19
- Wang, J. J., Vigan, A., Lacour, S., et al. 2021, *AJ*, 161, 148
- Weber, P., Benítez-Llambay, P., Gressel, O., Krapp, L., & Pessah, M. E. 2018, *ApJ*, 854, 153
- Wildt, R. 1939, *ApJ*, 90, 611
- Wright, A. E. & Barlow, M. J. 1975, *MNRAS*, 170, 41
- Wu, Y.-L., Bowler, B. P., Sheehan, P. D., et al. 2022, *ApJ*, 930, L3
- Zhu, Z., Andrews, S. M., & Isella, A. 2018, *MNRAS*, 479, 1850
- Zhu, Z., Nelson, R. P., Dong, R., Espaillat, C., & Hartmann, L. 2012, *ApJ*, 755, 6

- ¹ Departamento de Astronomía, Universidad de Chile, Casilla 36-D, Santiago, Chile
e-mail: oriana.dominguez@ug.uchile.cl
- ² Data Observatory Foundation, Eliodoro Yáñez 2990, Providencia, Santiago, Chile
- ³ Department of Physics, National Sun Yat-Sen University, No. 70, Lien-Hai Road, Kaohsiung City 80424, Taiwan, R.O.C.
- ⁴ Center of Astronomy and Gravitation, National Taiwan Normal University, Taipei 116, Taiwan
- ⁵ School of Physics and Astronomy, Sun Yat-sen University, Guangdong 519082, People's Republic of China
- ⁶ University of Santiago of Chile (USACH), Faculty of Engineering, Computer Engineering Department, Chile
- ⁷ Departamento de Física, Universidad de Santiago de Chile, Av. Víctor Jara 3493, Santiago, Chile
- ⁸ Millennium Nucleus on Young Exoplanets and their Moons (YEMS), Chile
- ⁹ Center for Interdisciplinary Research in Astrophysics and Space Exploration (CIRAS), Universidad de Santiago de Chile, Chile
- ¹⁰ Charles University, Faculty of Math and Physics, Astronomical Institute, V Holešovičkách 747/2, 180 00 Prague 8, Czech Republic
- ¹¹ Division of Space Research & Planetary Sciences, Physics Institute, University of Bern, Gesellschaftsstr. 6, 3012 Bern, Switzerland
- ¹² Max-Planck-Institut für Astronomie, Königstuhl 17, 69117 Heidelberg, Germany
- ¹³ Fakultät für Physik, Universität Duisburg-Essen, Lotharstraße 1, 47057 Duisburg, Germany
- ¹⁴ University Observatory, Faculty of Physics, Ludwig-Maximilians-Universität München, Scheinerstr. 1, 81679 Munich, Germany
- ¹⁵ Exzellenzcluster “Origins”, Boltzmannstr. 2, 85748 Garching, Germany
- ¹⁶ Institute for Computational Science, University of Zürich, Winterthurerstrasse 190, 8057 Zürich, Switzerland
- ¹⁷ ETH Zürich, Department of Physics, Wolfgang-Pauli-Strasse 27, 8093, Zürich, Switzerland